INL/RPT-24-78905

Development of Graphite Thermal and Mechanical Modeling Capabilities in Grizzly

May 2024

P. Bajpai[1]
V. Prithivirajan[1]
L. B. Munday[1]
G. Singh[1]
B. W. Spencer[1]

[1]Idaho National Laboratory

INL is a U.S. Department of Energy National Laboratory
operated by Batelle Energy Alliance, LLC

INL/RPT-24-78905

Development of Graphite Thermal and Mechanical Modeling Capabilities in Grizzly

P. Bajpai[1]

V. Prithivirajan[1]

L. B. Munday[1]

G. Singh[1]

B. W. Spencer[1]

[1]**Idaho National Laboratory**

May 2024

Idaho National Laboratory
Computational Mechanics and Materials
Idaho Falls, Idaho 83415

http://www.inl.gov

Prepared for the
U.S. Department of Energy
Office of Nuclear Energy
Under DOE Idaho Operations Office
Contract DE-AC07-05ID14517

Page intentionally left blank

ABSTRACT

Nuclear-grade graphites are used extensively in the core designs of multiple types of advanced nuclear reactors. In the reactor environment, graphite is exposed over long durations to extreme conditions, including high temperatures, radiation and potentially molten salt and oxygen. Exposure to these conditions can cause several degradation mechanisms in graphite, including nonuniform volumetric strains induced by irradiation and thermal expansion, which lead to stresses that can compromise the performance of graphite components. Evaluating component integrity, predicting component performance over the reactor lifetime, and developing design standards all require robust tools for predicting fracture initiation and propagation in graphite structural components in nuclear reactors. This report documents progress in an ongoing effort to develop modeling and simulation tools in the Grizzly code for predicting the performance of graphite exposed to reactor conditions. Recent developments include a set of thermal and mechanical models that now include the IG-110, NBG-18, and H-451 graphite grades. Improvements have also been made to a nonlinear damaged plasticity model applicable to predicting damage under tension and compression to quasibrittle materials, including graphite. In addition, enhancements have been made to the extended finite element method implementation targeted at simulating graphite fracture. These include new capabilities for crack nucleation in the interior of a solid body, improved treatment of crack nucleation on free surfaces, and more robust modeling approaches for crack growth approaching free surfaces or other cracks.

CONTENTS

1 INTRODUCTION

Graphite plays a prominent role in the core designs of multiple advanced reactor types being currently developed. It is used as a neutron reflector and moderator and has applications in high-temperature gas reactors, molten-salt reactors, fluoride-salt-cooled high-temperature reactors, and microreactors. The reactor environment, which exposes graphite to high temperature, radiation, and potentially molten salt and oxygen depending on the reactor type, can challenge graphite components in multiple ways.

To deploy graphite in nuclear reactor applications, it is important to predict its performance, accounting for the aforementioned effects of exposure to the reactor environment, under both normal and off-normal operating conditions. Computational simulation is an important tool for this purpose, but it is critical that any computational model be based on realistic properties obtained from experiments.

The Grizzly code [1] is an ideal platform for computational simulations of graphite performance. Grizzly is a code for the multiphysics simulation of the degradation and performance of structural components in nuclear power plants. It is based on the Multiphysics Object-Oriented Simulation Environment (MOOSE) framework [2], which is a finite-element based platform coupled physics models that facilitates solving large-scale problems on high-performance computing systems. A prior effort [3] demonstrated an initial capability to model graphite in Grizzly, with a focus on damage and fracture. An important limitation of that work is that, at that time, the set of material property models was quite limited, and as a result, a mixture of property models for multiple grades was used in the demonstration. That initial work also demonstrated the ability to model fracture and damage using multiple modeling approaches, but improvements were needed in those capabilities.

This effort advances the previously initiated efforts for graphite modeling in the U.S. Department of Energy's Nuclear Energy Advanced Modeling and Simulation (NEAMS) program in three main areas:

- **Thermal and mechanical models for graphite grades:** The present effort expands on the set of thermal and mechanical models for graphite in Grizzly to include multiple grades. It completed the set of models for H-451, which was previously partially implemented. In addition, it developed thermal and mechanical models for IG-110 and NBG-18, both of which are highly relevant for current advanced reactor development. While analytic expressions were already available for H-451, that was not the case for the other two grades. Analytic expressions for irradiation-induced dimensional change and irradiation-induced creep were fitted to experimental data, and models were implemented based on those expressions.
- **Damaged plasticity model development:** In the prior effort, a damaged plasticity model that was originally developed for concrete was found to reasonably predict the nonlinear compressive response of graphite. While that model was able to simulate the response of a splitting tension test, there were still a number of issues with the implementation of that model. In the present work, the implementation of that model was thoroughly reviewed and revised to better match the paper it is based on. In addition, an initial implementation of a viscoplastic regularization technique to improve the numerical stability of that model was developed.
- **XFEM capability development for graphite fracture:** The extended finite element method (XFEM) was improved in a number of ways in the prior work and was applied to simulate fracture propagation in a graphite component. In the current effort, the XFEM implementation in MOOSE has been updated to improve its handling of crack initiation on free surfaces of a model, permit crack initiation in the interior of a model, and improve the behavior of cracks propagating toward a surface of a model.

The following sections of this report document these developments, in the order listed.

2 THERMAL AND MECHANICAL MODEL DEVELOPMENT FOR RELEVANT GRAPHITE GRADES

To predict the in-service performance of graphite components in a nuclear reactor, it is essential to have models for the thermal and mechanical properties of the graphite grade being used. In many cases, the most significant contributors to stresses in those components are eigenstrains and creep strains. The properties influencing these phenomena can vary significantly between graphite grades, so properties for the specific grade being employed are essential.

The total strain, ε, in graphite components subjected to irradiation in a reactor core is a function of the irradiation dose, γ, temperature, T, and applied stress, σ. The total strain can be expressed as:

$$\varepsilon = \varepsilon^E + \varepsilon^T + \varepsilon^R + \varepsilon^C, \tag{1}$$

where ε^E is the elastic strain, ε^T is the thermal strain, ε^R is the irradiation-induced dimensional change (IIDC) strain, ε^C is the creep strain. The creep strain is given as:

$$\varepsilon^C = \varepsilon^p + \varepsilon^s, \tag{2}$$

where ε^p and ε^s are the primary and secondary creep strains, respectively.

The experimentally determined strain in a graphite sample subjected to creep testing is conventionally defined as:

$$\varepsilon = \frac{l - l_\circ}{l_\circ}, \tag{3}$$

where l and $l_\circ$ denote the linear dimensions of the sample before and after the test. Modeling creep behavior in graphite requires models for each of the deformation mechanisms.

To facilitate simulation of graphite reactor components, a set of thermal and mechanical models for graphite grades relevant to advanced reactors is being developed in Grizzly. These are implemented in the following set of classes in Grizzly:

- `GraphiteThermalGaseous`: Computes thermal properties (thermal conductivity and specific heat) as well as properties pertaining to the transport of gaseous species
- `StructuralGraphiteCreepUpdate`: Computes irradiation creep strains
- `StructuralGraphiteElasticityTensor`: Computes the temperature- and fluence-dependent elasticity matrix
- `StructuralGraphiteIrradiationEigenstrain`: Computes irradiation-induced dimensional change
- `StructuralGraphiteThermalExpansionEigenstrain`: Computes thermal expansion strains

Each of these classes provides models for a growing set of graphite grades. Prior to the current effort, models were only available for H-451, a grade that has been extensively characterized and for which analytic expressions for most properties were already available.

The present effort focused on supporting a larger set of graphite grades. Models have been developed for IG-110 and NBG-18, both of which are being experimentally characterized in the U.S. Department of Energy's advanced graphite creep (AGC) program. For both of these grades, analytic expressions were not available, so much of the present effort to develop models for the various properties described in the following sections was devoted to developing analytic expressions based on experimental data.

2.1 Thermal Properties

The main properties needed to model the thermal response of graphite components are the specific heat at a constant pressure, C_p, and the thermal conductivity, k. Both of these vary by graphite grade and are functions of temperature. Models were previously implemented for the H-451 and IG-110 grades, so the current effort developed models for NBG-18.

For NBG-18, the temperature dependence of thermal conductivity of unirradiated samples has been calculated previously by [4]. The typical trend for graphites, of decreasing thermal conductivity with temperature, is evident, and the thermal conductivity takes the form:

$$k = 145.8 - 0.1619T + 1 \times 10^{-4}T^2 - 2 \times 10^{-8}T^3, \tag{4}$$

where k denotes the thermal conductivity in $\mathrm{W\,m^{-1}\,K^{-1}}$ and T is the temperature in °C. This function is shown in Figure 1.

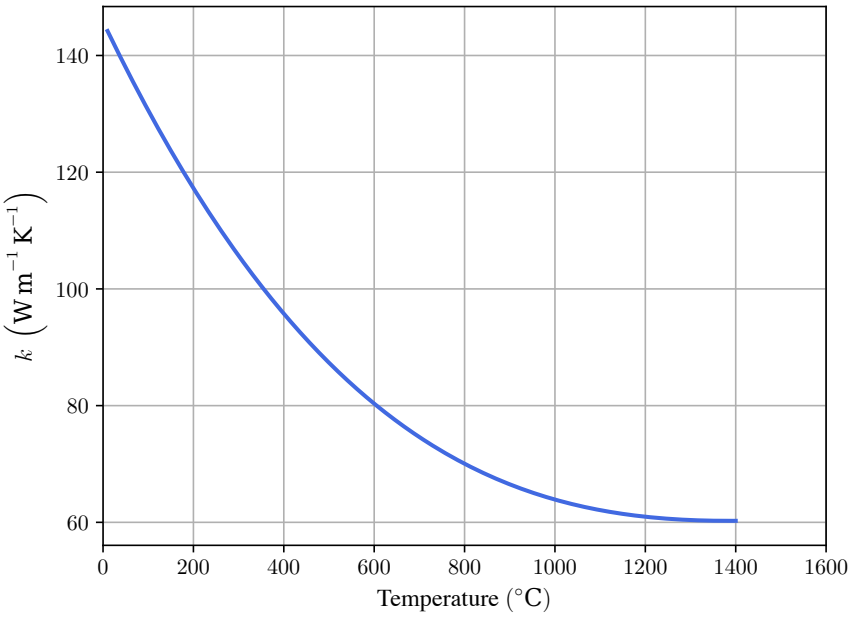

Figure 1: Temperature dependence of thermal conductivity of NBG-18 as modeled by [4].

2.2 Elasticity and Thermal Expansion

The thermal expansion coefficients and elastic properties also vary by graphite grade and depend on temperature and radiation. For NBG-18, the coefficient of thermal expansion has been calculated by [5] and [6] and is summarized by [7]. For elastic properties, [8] have used a Weibull distribution with a mean static elastic modulus of 10.44 GPa and a standard deviation of 0.95 GPa.

Irradiation increases the coefficient of thermal expansion (CTE) of NBG-18, with both irradiation dose and irradiation temperature affecting the level of increase [7]. For the unirradiated samples, the CTE has been calculated by [4] as:

$$\beta = 1.24 + 2.0 \times 10^{-3}T - 4.0 \times 10^{-7}T^2 \tag{5}$$

where the CTE, β, is in $1 \times 10^{-6}\,\mathrm{K}^{-1}$ and temperature T is in °C. For the irradiated case, albeit for an unspecified dose, the expression given by [9] is:

$$\beta = 4.10 + 1.4 \times 10^{-3} T \tag{6}$$

where the CTE, β, is in $1 \times 10^{-6}\,\mathrm{K}^{-1}$ and temperature T is in °C. The temperature dependence of the CTE for unirradiated and irradiated graphite are shown in Figure 2.

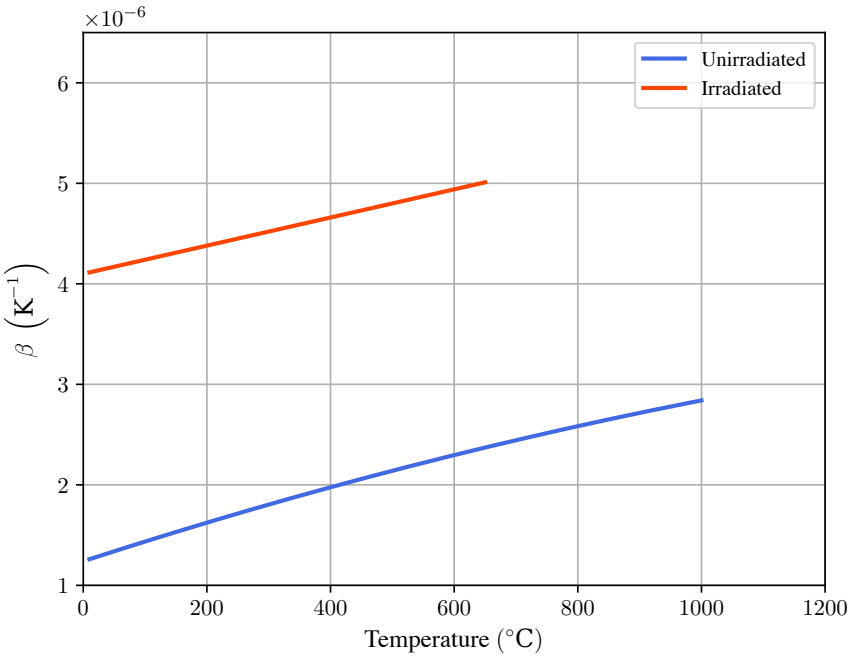

Figure 2: Temperature dependence of CTE of unirradiated and irradiated NBG-18 as modeled by [4] and [9].

Though paragraph *(d)* of Article HHA-II-4100 of Section III Rules for Construction of Nuclear Facility Components Division 5 High Temperature Reactors of the American Society of Mechanical Engineers (ASME) Boiler and Pressure Vessel Code states that "the effect of creep strain on coefficient of thermal expansion and elastic modulus shall be determined and included in the Material Data Sheet" [10], such a model has not been developed as part of this work due to the limitations of the available experimental data.

2.3 Irradiation-Induced Dimensional Change

Fast neutrons (with energy, E_n, in the range $1\,\mathrm{eV} < E_n < 10\,\mathrm{MeV}$) impinging on graphite components knock out the carbon atoms from their equilibrium positions, creating lattice vacancies and carbon interstitials. The primary knock-on atoms cause a cascade effect as they collide with neighboring carbon atoms. Such cascade atoms, called secondary knock-on atoms, are usually clustered in groups of 5–10 atoms, and the displacements are often treated as occurring randomly. The neutron energy spectrum and the neutron flux affect the total number of displaced atoms, which then recoil through the graphite lattice. Though most of the displaced atoms recombine with the vacancies, a process dependent on the temperature of irradiation, others can coalesce, forming the nuclei of dislocation loops. With further irradiation, interstitial clusters can be destroyed by irradiation annealing, and lattice vacancies in the same layer can collapse parallel to the layers,

forming sinks for other vacancies, which are increasingly mobile over 600 °C and can no longer combine and annihilate interstitials [11]. While several deformation mechanisms have been proposed for irradiated graphite, see [12–14] for example, they all suggest that crystallite dimensional change results from carbon atom displacements. Interstitials cause crystallite growth along the *c*-axis while coalescing vacancies, which leads to shrinkage along the *a*-axis.

Nuclear graphite is polycrystalline with significant texture and contains thermal-shrinkage cracks formed during the manufacturing process. These cracks are preferentially aligned with the crystallographic *a*-axis and initially accommodate the *c*-direction expansion. As a result, a primarily *a*-dimension contraction is observed and the graphite goes through a volumetric shrinkage. As the neutron dose increases, new porosity is formed and the volume shrinkage rate falls, eventually dropping to zero. Upon further irradiation, beyond this point, graphite starts to expand at an increasing rate as the irradiation dose increases. This change from volumetric contraction to expansion is known as *turnaround*, and due to the differential crystal strain, the expansion continues, accompanied by the generation of cracks and pores in graphite and eventual disintegration. The structural and dimensional changes in polycrystalline graphite are thus a function of crystallite dimensional changes and the graphite's texture, which in turn depend on the fabrication method [11].

In addition to governing the rate of vacancy coalescence mentioned previously, temperature also plays a key role in the turnaround process. The thermal closure of internal porosity that is aligned with the *a*-direction and accommodates the *c*-direction swelling is dependent on the irradiation temperature. At higher irradiation temperatures, a greater fraction of the porosity closes, and therefore, the turnaround occurs with lower shrinkage and at a lower dose. This implies that the turnaround dose follows an Arrhenius-like behavior as a function of temperature. A generalized theory of dimensional change can be found in [15–17].

2.3.1 Irradiation-Induced Dimensional Change Modeling

The IIDC in graphite is often empirically modeled as a set of piecewise quadratic functions of irradiation dose. The piecewise functions apply to specific temperatures and often deviate from the true behavior if the temperature changes. However, as mentioned previously, the turnaround dose appears to follow an Arrhenius-like behavior with respect to temperature. In this work, this behavior has been taken advantage of to include the effect of temperature in the expression for the IIDC.

Using the vertex formulation, the IIDC strain ε^R can be represented as:

$$\varepsilon^R = a_1 \left(\gamma - \gamma^{\mathrm{TA}}\right)^2, \tag{7}$$

where the turnaround dose, γ^{TA}, is represented as:

$$\gamma^{\mathrm{TA}} = a_2 \exp\left(-E_a/k_B T\right), \tag{8}$$

with E_a representing the activation energy and $k_B = 8.617333262 \times 10^{-5}\mathrm{eV\,K^{-1}}$ denoting the Boltzmann constant. Expanding Equation (7) and applying the condition that $\varepsilon^R = 0$ for $\gamma = 0$, one obtains the following functional form that can be fit to the data obtained from experimental campaigns:

$$\varepsilon^R = a_1\gamma^2 + a_2 \exp(E_a/k_B T)\gamma. \tag{9}$$

In the AGC campaign, several nuclear-grade graphites have been studied and several properties have been measured, including IIDC. As part of the irradiation-induced creep measurements, mechanical loads (inducing mechanical strain within the graphite) of varying levels are applied to some of the specimens,

while other specimens are left unloaded. The unloaded specimens, when irradiated, undergo IIDC and can be used to determine the parameters a_1 and a_2 in Equation (9). This process was applied to both IG-110 and NBG-18 graphite grades.

The input-space mappings to demonstrate the conditions for which the experimental data is currently available are shown in Figures 3 and 4. From these, it is evident that while the load stresses are relatively well clustered around the design stresses of 0.0 , 13.8 , 17.2 , and 20.7 MPa, the irradiation temperatures of the samples are significantly spread out.

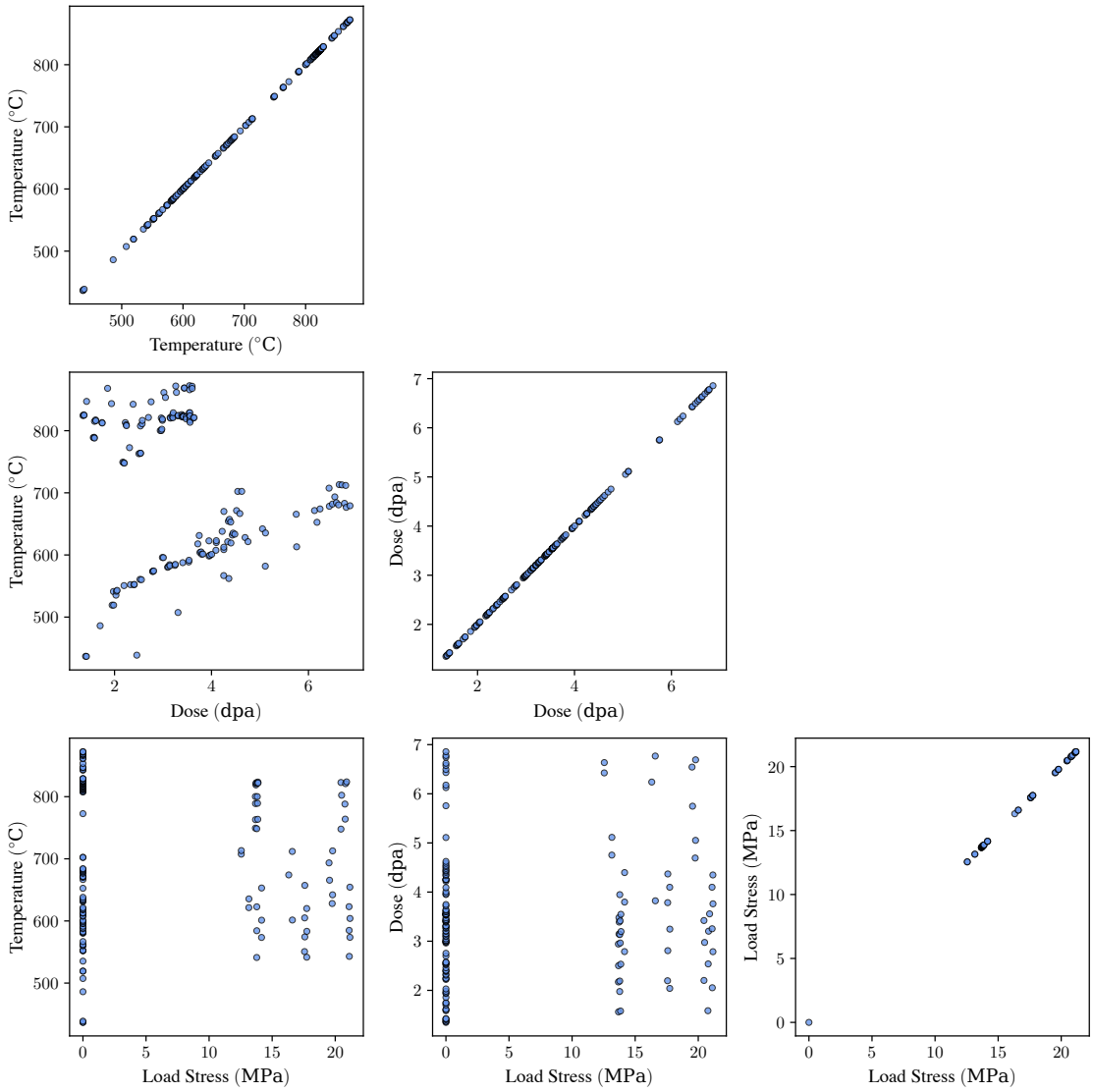

Figure 3: Analysis of the input space for the IG-110 samples evaluated in the AGC campaign.

The experimental data for the dimensional change in both the axial and transverse directions are shown in Figures 5 to 8. In the axial direction (i.e., the direction of applied compressive load), the samples are shortened. As the load is increased, irradiation-induced creep further reduces the axial length of the samples. As expected, irradiation dose directly impacts the total strain observed in the samples. However, the irradiation doses in the AGC 1–3 campaigns are not high enough to reach the turnaround point. In the transverse directions, there is a similar behavior to that in the axial direction (i.e., a decrease in length in

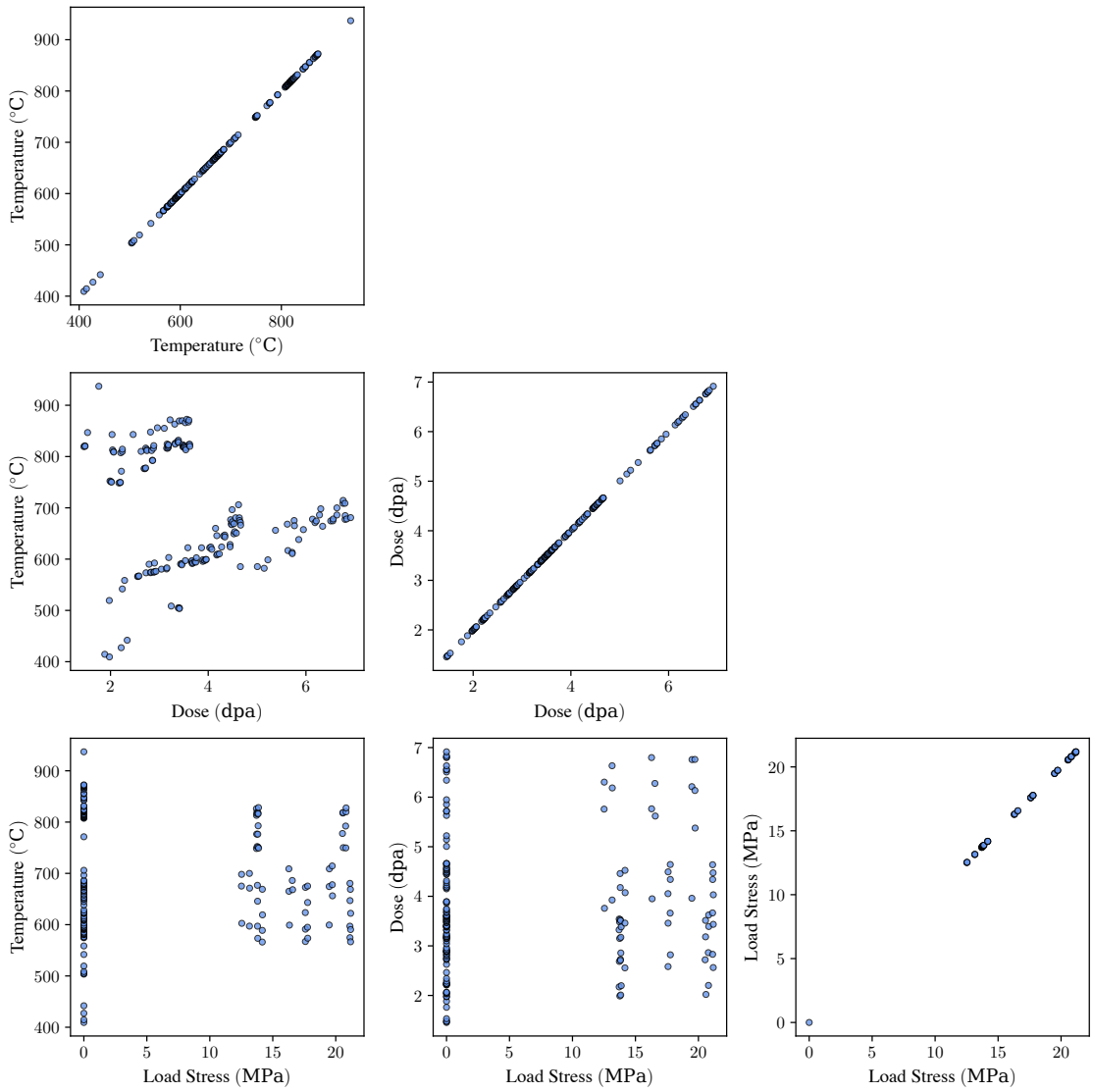

Figure 4: Analysis of the input space for the NBG-18 samples evaluated in the AGC campaign.

the diametral direction) for the unloaded specimens. However, under compressive loading, creep leads to an increase in sample diameter.

For the purpose of determining an expression to quantify IIDC, the non-loaded samples shown in Figures 9 and 10 are used. IIDC in both directions demonstrate good agreement, so the combined data set can be used to obtain a fitted function for the IIDC. No discernible effect of temperature was observed, see Figures 11 and 12, and in the absence of high enough doses to observe turnaround, the known Arrhenius-like behavior of turnaround was assumed to be true.

The IIDC model for IG-110 calibrated from the experimental data obtained in three irradiation experiments of the AGC program is expressed as:

$$\varepsilon^R = 1.8391 \times 10^{-3}\gamma^2 - 1.3592 \times 10^{-2} \exp\left(1.4663 \times 10^{-2}/k_B T\right)\gamma \tag{10}$$

where γ (1×10^{26} n/m^2) is the fast neutron fluence, the activation energy E_a is assumed to be in eV, and T is the temperature in Kelvin. The above functional form captures the IIDC behavior in the pre-

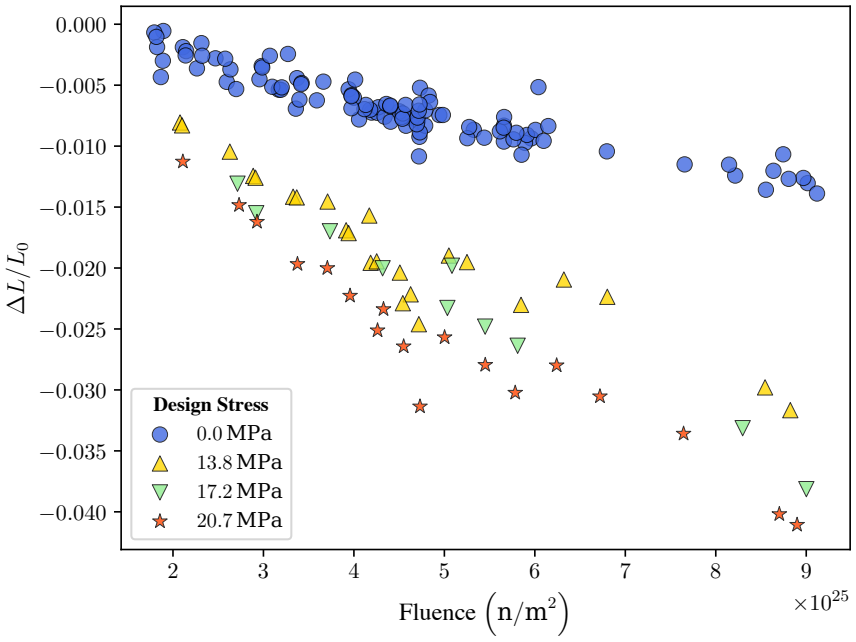

Figure 5: Axial strain of the IG-110 graphite samples as measured by AGC 1–3 campaigns.

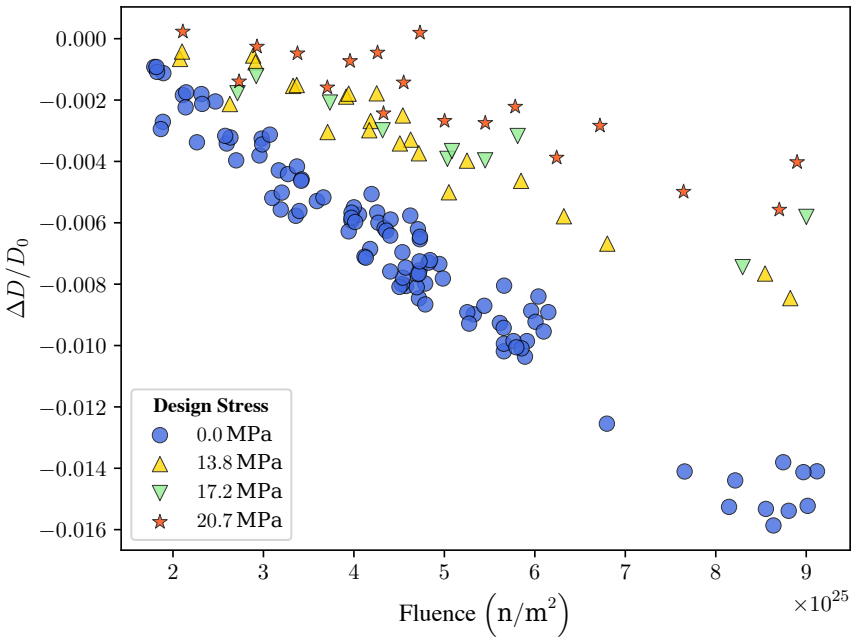

Figure 6: Transverse strain of the IG-110 graphite samples as measured by AGC 1–3 campaigns.

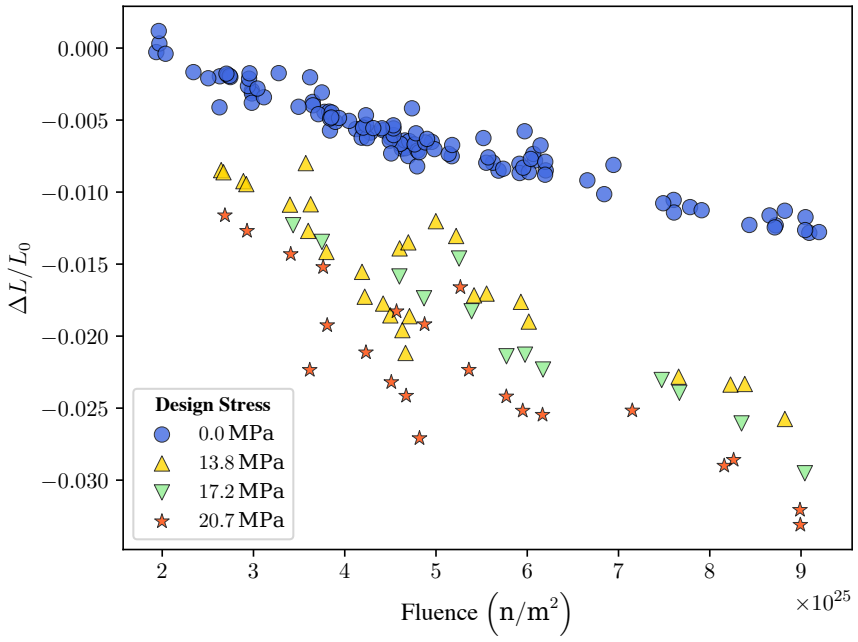

Figure 7: Axial strain of the NBG-18 graphite samples as measured by AGC 1–3 campaigns.

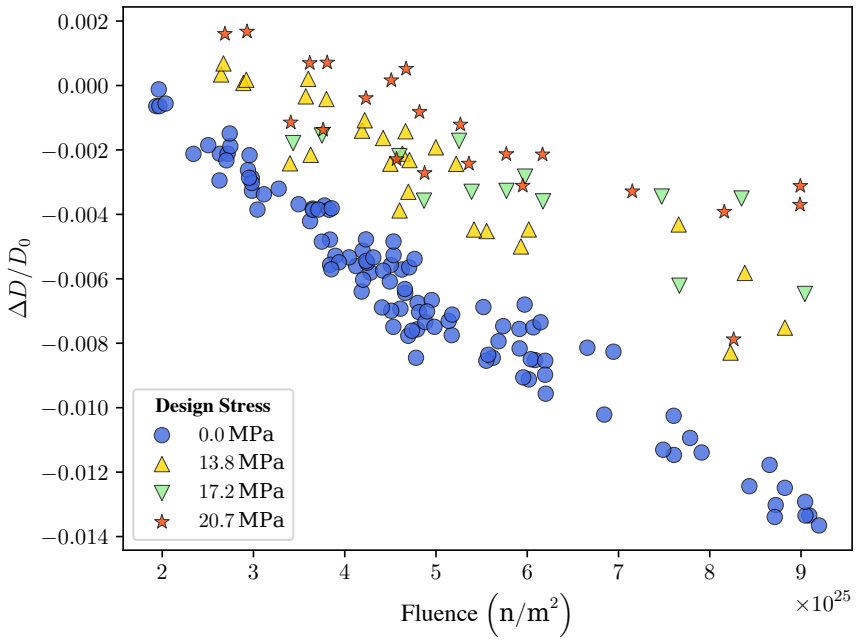

Figure 8: Transverse strain of the NBG-18 graphite samples as measured by AGC 1–3 campaigns.

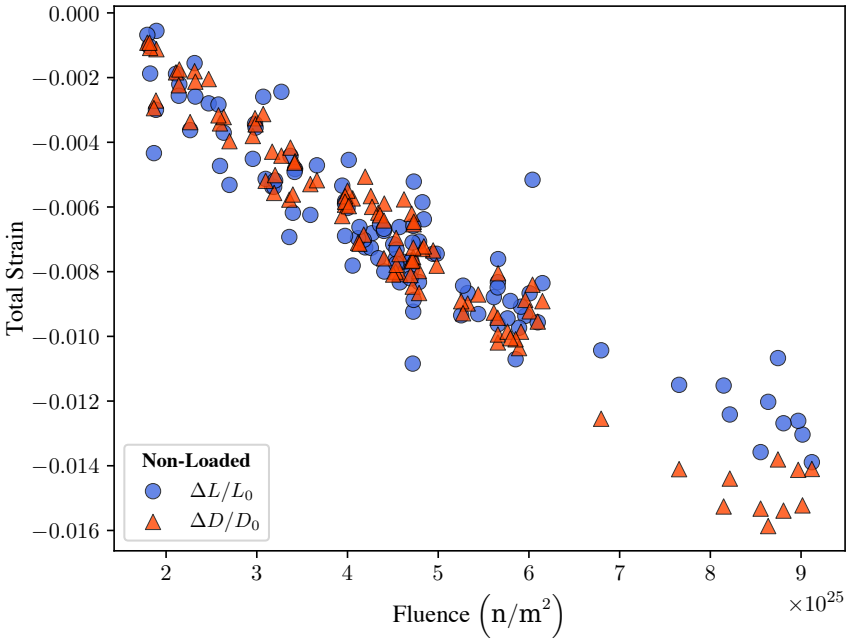

Figure 9: Comparison of the axial and transverse dimensional changes of IG-110 for non-loaded specimens.

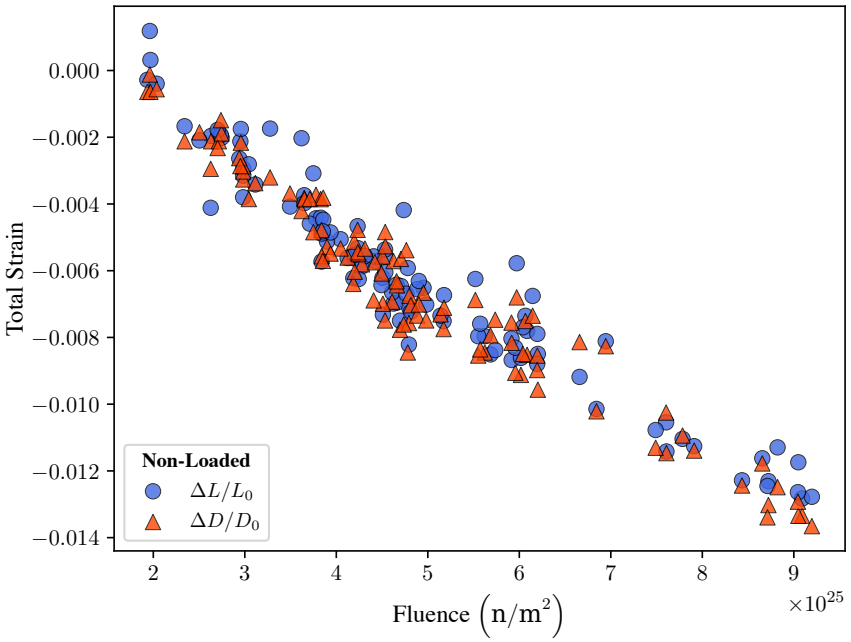

Figure 10: Comparison of the axial and transverse dimensional changes of NBG-18 for non-loaded specimens.

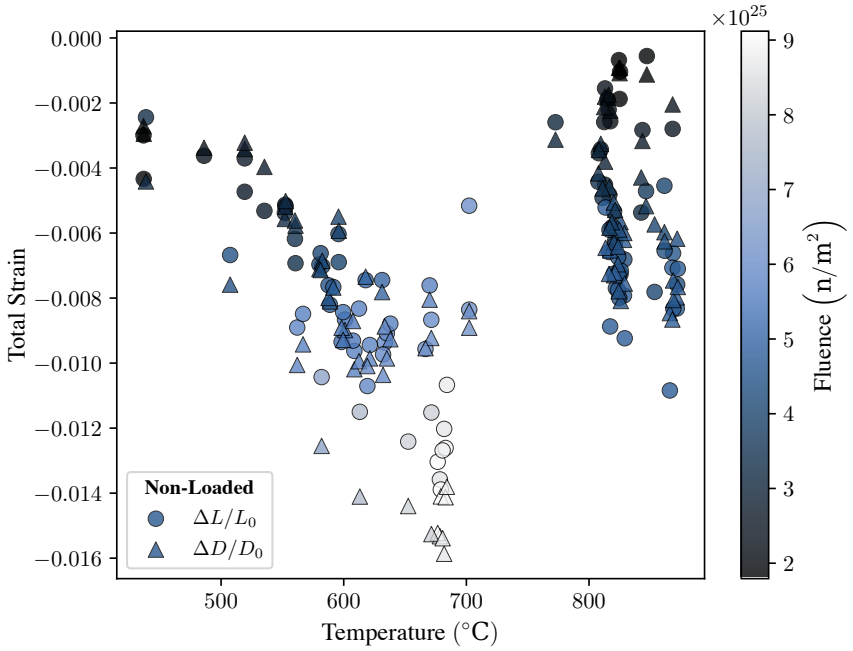

Figure 11: Temperature dependence of the axial and transverse dimensional changes of IG-110 for non-loaded specimens.

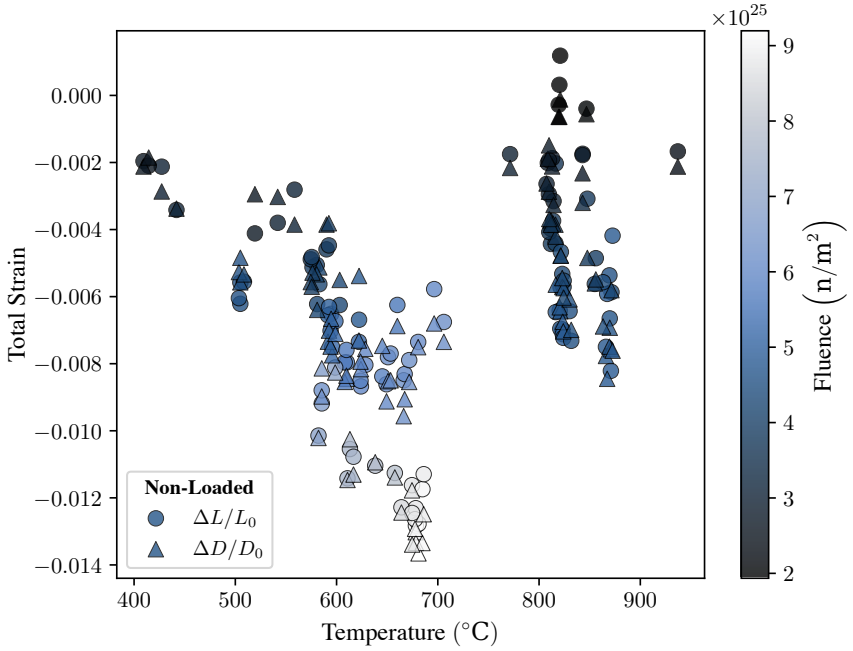

Figure 12: Temperature dependence of the axial and transverse dimensional changes of NBG-18 for non-loaded specimens.

Table 1: Empirical coefficients a_1 and a_2 for IIDC of IG-110 graphite by [18].

	400 °C	600 °C	800 °C
a_1	0.279	0.450	0.821
a_2	-1.64	-1.86	-2.19

turnaround regime and, when compared with the experimental results, follows the trend of the data as shown in Figure 13. The model does not exactly match the experimental data, which is a consequence of the spread in the experimental observations. Characterizing the uncertainty in the model predictions, including identifying the sources of the uncertainty, needs further research.

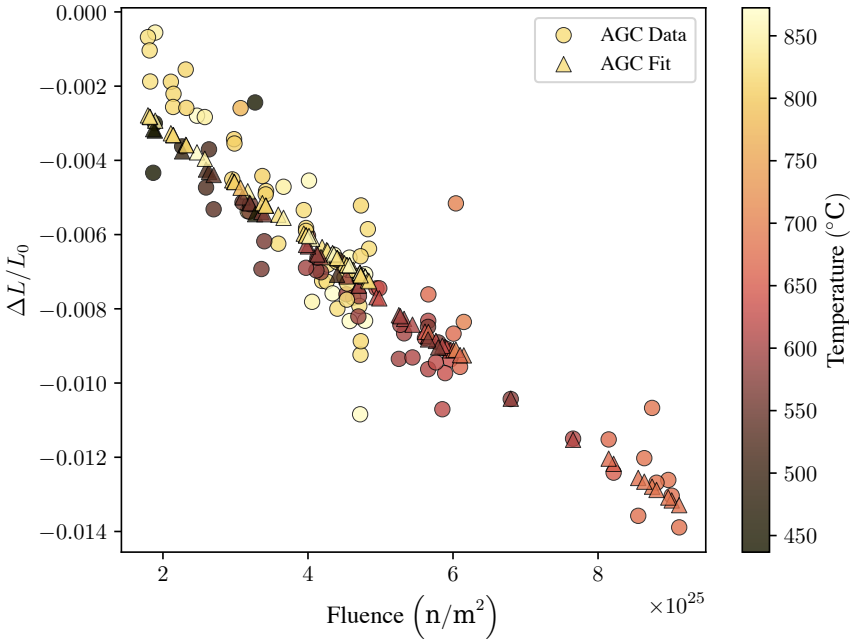

Figure 13: Comparison of the IIDC strain predictions with experimental data for IG-110 graphite.

An alternative model for IG-110 IIDC has previously been presented by [18], and this model has been added to Grizzly as an alternative to the presently developed model. In the Shibata model, the IIDC is defined as:

$$\varepsilon^R = a_1\gamma^2 + a_2\gamma, \tag{11}$$

where a_1, a_2 are empirical coefficients defined for specific values of temperature. These values, as reported by [18], are shown in Table 1. In the absence of a continuous function describing IIDC, the calculations based on the Shibata model must use interpolations for temperatures between those for which functional forms for IIDC were developed.

When comparing the predictions of the Shibata model with the experimental data and predictions from the current work, shown in Figure 14, the Shibata model overestimates the IIDC strain compared to both the experimental data and the predictions of this work. As a result, as shown in Figure 15, the Shibata model produced higher errors compared to the model developed here.

For NBG-18 graphite, a similar procedure for calibrating the parameters was adopted, albeit with a linear formulation because the fluences for the experimental data did not closely enough approach turnaround to

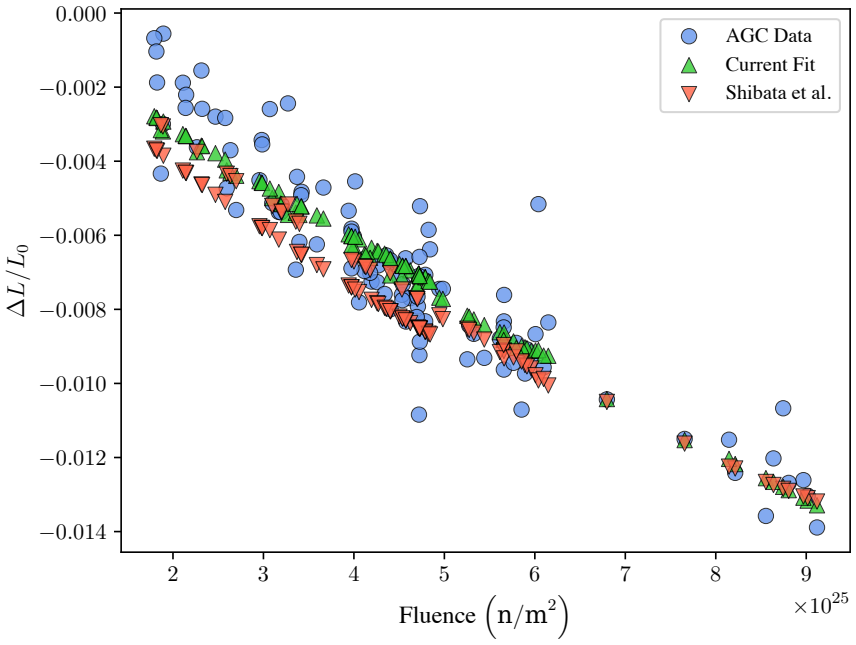

Figure 14: Comparison of IIDC for IG-110 graphite between the model fitted in this work, the Shibata model, and experimental data.

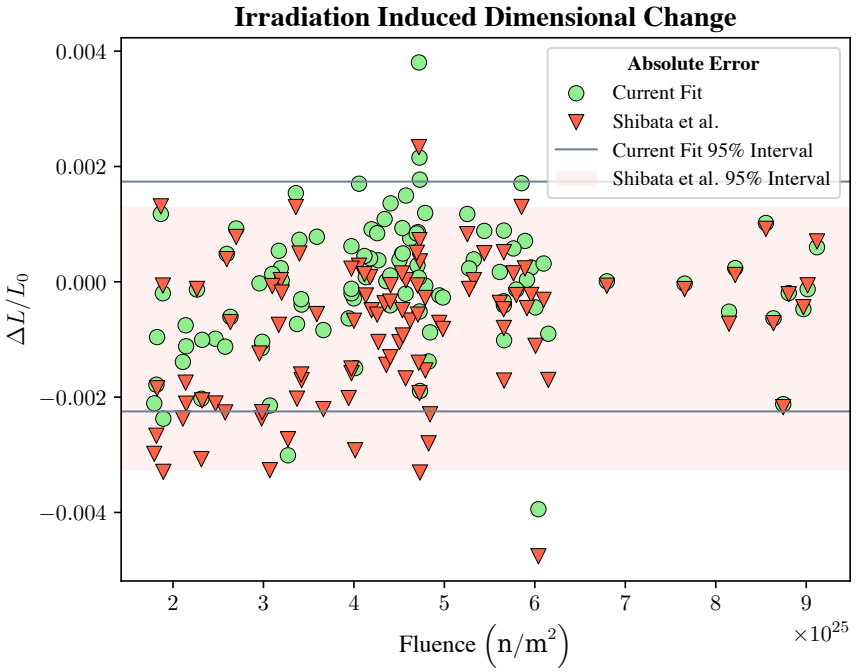

Figure 15: IIDC error comparison between the model from this work and the Shibata model with respect to experimental observations of IG-110 graphite.

indicate the concavity expected to be observed under higher fluences. The calibration yielded the following expression for IIDC of NBG-18:

$$\varepsilon^R = -1.31946472 \times 10^{-2}\gamma - 2.98735160 \times 10^3 \exp\left(3.04143838 \times 10^2 / k_B T\right)\gamma \tag{12}$$

with the symbols taking the same form as before. Equation (12) results in a linear approximation of the IIDC as shown in Figure 16 and the errors are shown in Figure 17. Though the linearity of the fit results in a higher error for low dose ranges, the overall error is low compared to the experimental observations. As more experimental data becomes available, the model will be recalibrated to capture the nonlinearity expected with increasing fluence.

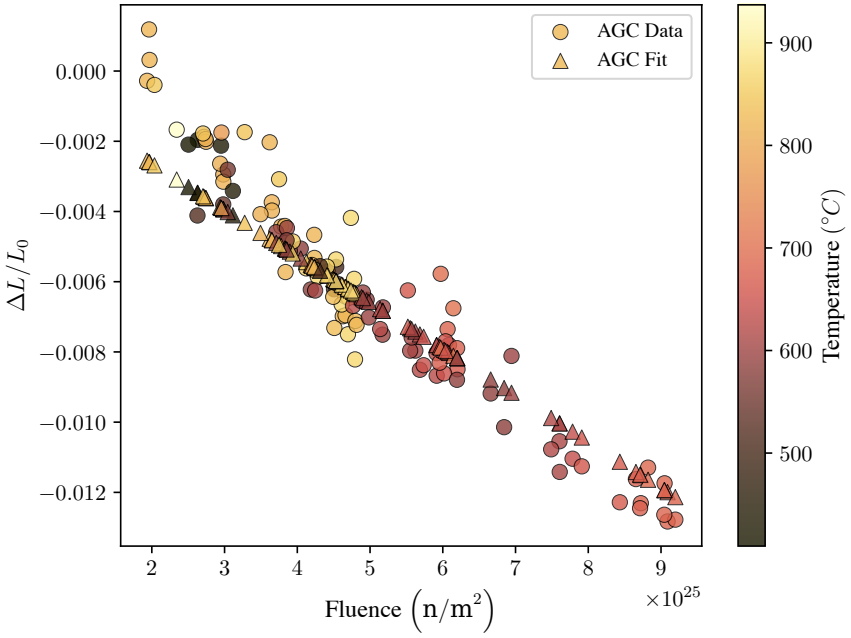

Figure 16: Comparison of the IIDC strain predictions with experimental data for NBG-18 graphite.

2.4 Irradiation Creep

Kelly and Foreman [19] proposed a mechanism that explains how irradiation affects the creep behavior of graphite. They postulated that neutron irradiation creates basal plane pinning and unpinning sites in the crystals. Depending on the irradiation dose and temperature, either full or partial pinning may occur, but since the pinning points are interstitial clusters of 2–6 atoms [20], they are annealed (destroyed) by further irradiation. Thus, irradiation releases dislocation lines from their original pinning sites, enabling the crystals to flow as a result of basal plane slip at a rate determined by the rate of pinning and unpinning of dislocations [11]. Kelly and Foreman's theory assumes that polycrystalline graphite consists of a single phase with true and apparent densities ρ_0 and ρ. Within the elementary regions of the material, which can be assumed to be monocrystalline, stress remains uniform, and with basal slip as the only possible deformation mechanism, the strain rate is determined by:

$$\dot{\epsilon}_{xz} = k\left(\sigma_{xz}\right)\phi, \tag{13}$$

and

$$\dot{\epsilon}_{yz} = k\left(\sigma_{yz}\right)\phi, \tag{14}$$

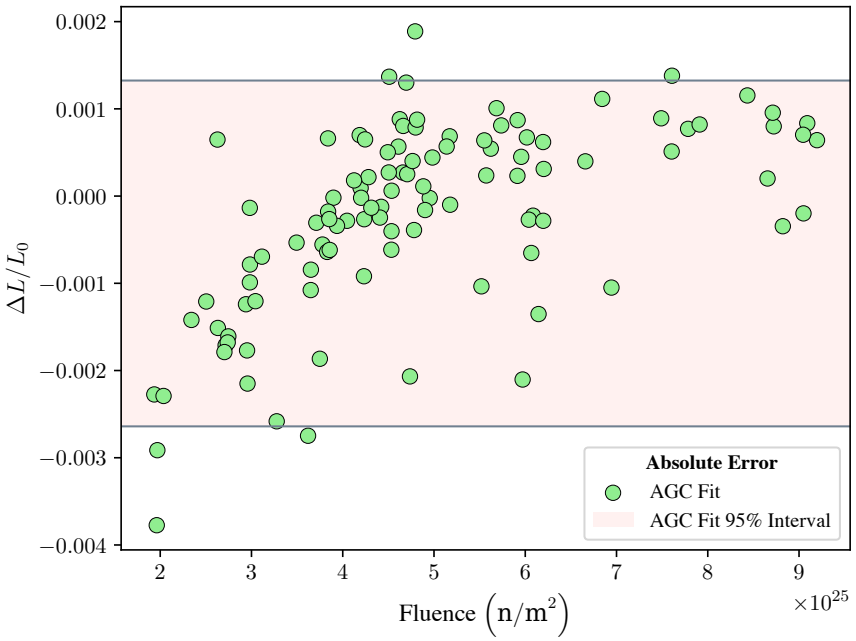

Figure 17: IIDC prediction error with respect to experimental observations for NBG-18 graphite.

where ϕ is the fast neutron flux, k is the steady-state creep coefficient, and σ is the stress in the given direction. The dislocation-line flow model uses the flexible line approach where the dislocation line is pinned or unpinned and the dislocation-line bowing is a function of the line tension and pin spacing. As the pinning site concentration increases under irradiation from the initial value to a steady-state concentration, the creep rate goes from an initial high value to a lower steady-state value as the pinning concentration saturates. Thus, a two-stage model can be envisioned wherein the primary creep rate is initially high and falls to a secondary or steady-state creep rate. The steady-state creep term should be dominant when the dose has reached values at which physical property changes due to dislocation pinning have saturated [11]. At higher temperatures, the secondary creep rate, k, will increase due to the incompatibility of crystal strains increasing the internal stresses as well as additional effects due to the destruction of interstitial pins by the thermal diffusion of vacancies. Furthermore, Kelly and Foreman suggest that nonlinear creep at high stress levels is related to the high-dose dimensional change behavior of polycrystalline graphite.

Irradiation-induced creep strain is the difference between the dimensional change of a stressed specimen and an unstressed specimen irradiated under identical conditions. The *linear viscoelastic* creep model conforms to the Kelly–Foreman theory of creep with an initially large primary creep coefficient, while the dislocation pinning sites develop to the equilibrium concentration, at which time the creep coefficient has fallen to the steady-state or secondary value. The total creep strain ε^C is therefore defined as:

$$\varepsilon^C = \frac{a\sigma}{E_0}\left[1 - \exp\left(-b\gamma\right)\right] + k\sigma\gamma, \tag{15}$$

where σ denotes the applied stress, E_0 represents the initial (preirradiated) Young's modulus, γ is the fast neutron fluence, a and b are constants with a usually being one, and k is the secondary creep coefficient. Experimentally, the primary creep saturated at approximately the elastic strain, σ/E_0. Assuming this is the case reduces Equation (15) to:

$$\varepsilon^C = \frac{\sigma}{E_0} + k\sigma\gamma, \tag{16}$$

As suggested by [9], the linear viscolastic model can be used for modeling creep of graphite with sufficient accuracy, and that model has been adopted in this work. It should be noted that other models, summarized in [11], have also been proposed.

2.4.1 Creep Modeling

In the AGC experiments, mechanically loaded (i.e., stressed) specimens were designated as the creep specimens, and the unloaded (unstressed) specimens were designated as the control specimens. The difference in dimensional change between the loaded and unloaded specimens (assuming that temperature and dose levels are the same) provides the amount of irradiation-induced creep strain for the graphite specimens. From this strain level, a creep rate for each graphite grade can be calculated as a function of dose if both specimens were irradiated at the same constant temperature and dose level. The AGC experiment is designed to measure the constant creep strain behavior (secondary creep) of the various grades. The experiment assumes that the induced creep strain for all specimens is within the secondary creep regime; therefore, it behaves linearly with respect to received neutron dose [9].

The fitting of parameters for both IG-110 and NBG-18 irradiation-induced creep follows a process similar to that described for IIDC. Firstly, the IIDC strain, computed using the fitted functional form developed in the previous section for the graphite grade considered, is subtracted from the experimental data to obtain the creep contribution. The secondary creep coefficient is then fitted to that IIDC-corrected experimental strain based on the following functional form to include the temperature effect:

$$\varepsilon^C = \frac{\sigma}{E_0} + a_1 \exp\left(a_2 T\right) \sigma\gamma \tag{17}$$

where a_1 and a_2 are the parameters that must be determined.

Based on nonlinear least-squares fitting, the following functional form of irradiation-induced creep is obtained for IG-110 graphite:

$$\varepsilon^C = \frac{\sigma}{E_0} - 3.3367 \times 10^{-4} \exp\left(1.60542 \times 10^{-3} T\right) \sigma\gamma \tag{18}$$

where the preirradiation Young's modulus of IG-110 is temperature-dependent and takes the form based on [18]:

$$E_0 = 9.98 - 8 \times 10^{-4} T + 2 \times 10^{-6} T^2 \tag{19}$$

where T denotes the temperature in °C and E_0 is in GPa. The temperature dependence of Young's modulus is illustrated in Figure 18. The irradiation creep predictions based on the model obtained in this work show good agreement with the experimental data as can be seen in Figure 19. It must be noted that the results show the combined contribution from IIDC and irradiation-induced creep. The deviation between the predicted and experimental strains is a direct consequence of the variation in experimental data, and accounting for these deviations will require the use of stochastic models capable of uncertainty quantification.

Similar to IIDC, the model from [18] has been included as an option in Grizzly. The secondary creep coefficient used in the Shibata model is given as:

$$k = 7.163 \times 10^{-4} \exp\left(0.0012 T\right), \tag{20}$$

where temperature T is in °C. It has been suggested by [21] that the Shibata model undervalues the creep coefficient at low temperatures. The predictions from the current work have been compared with the results from the Shibata model, and the comparisons and errors are shown in Figures 20 and 21, respectively. The

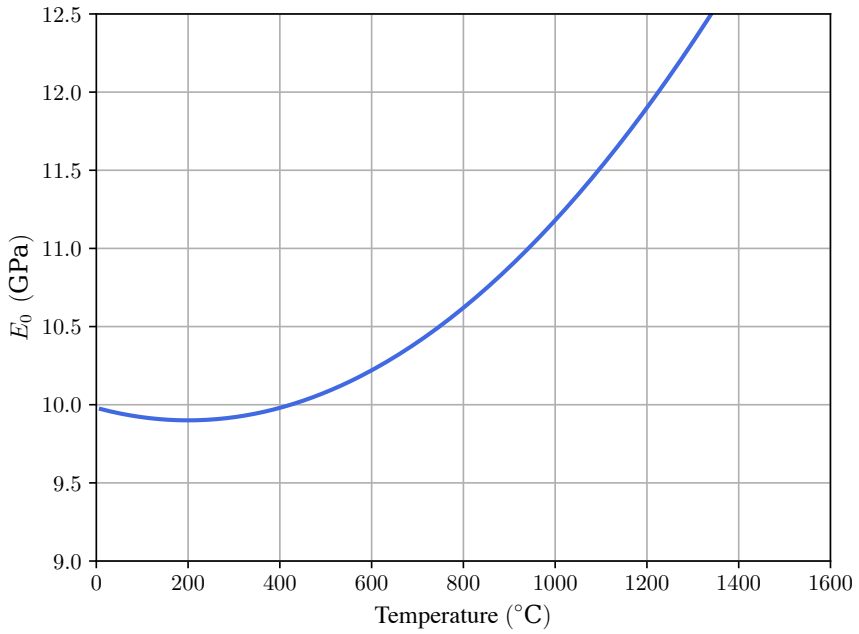

Figure 18: Temperature dependence of Young's modulus for IG-110 graphite.

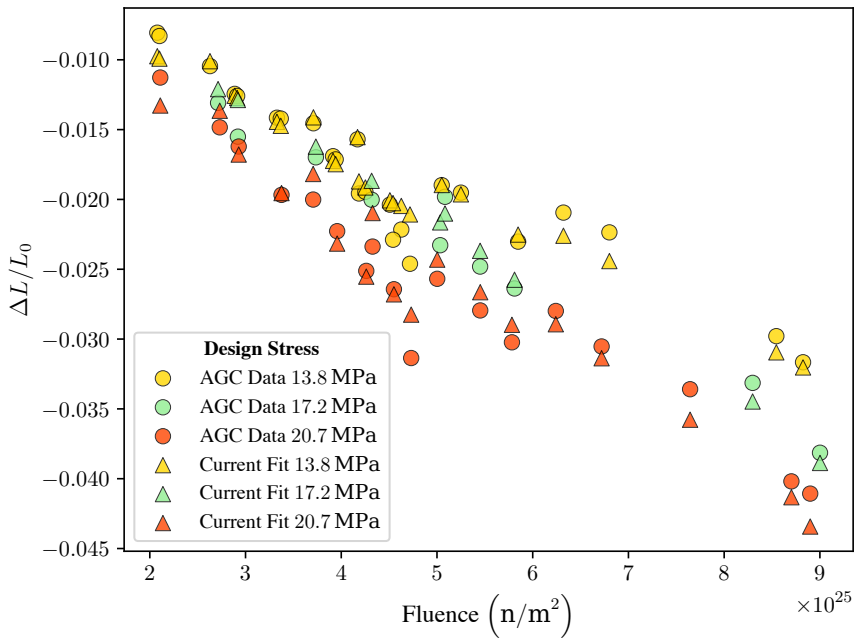

Figure 19: Comparison of the creep strain predictions from the currently developed fit with experimental data for IG-110 graphite.

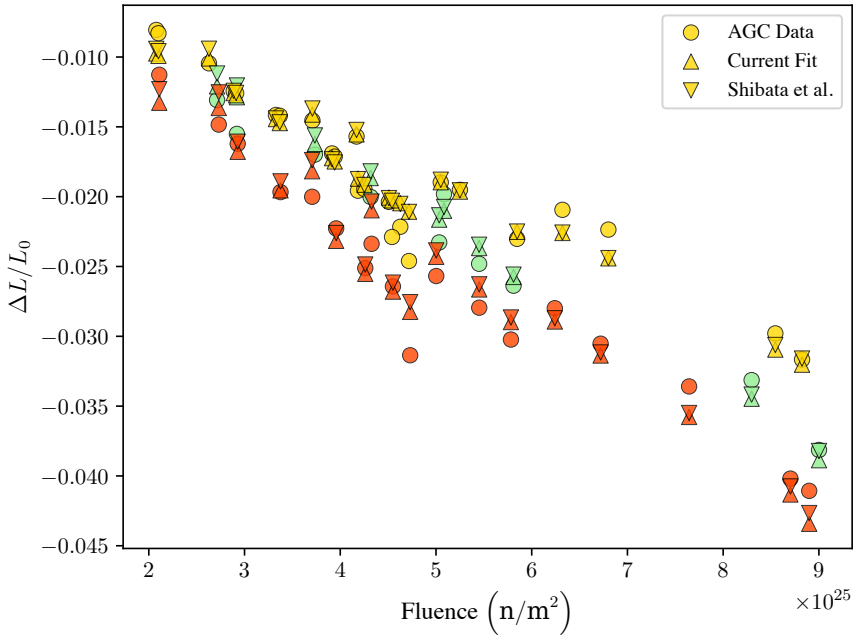

Figure 20: Comparison of the creep strain predictions from the Shibata model with experimental data for IG-110 graphite.

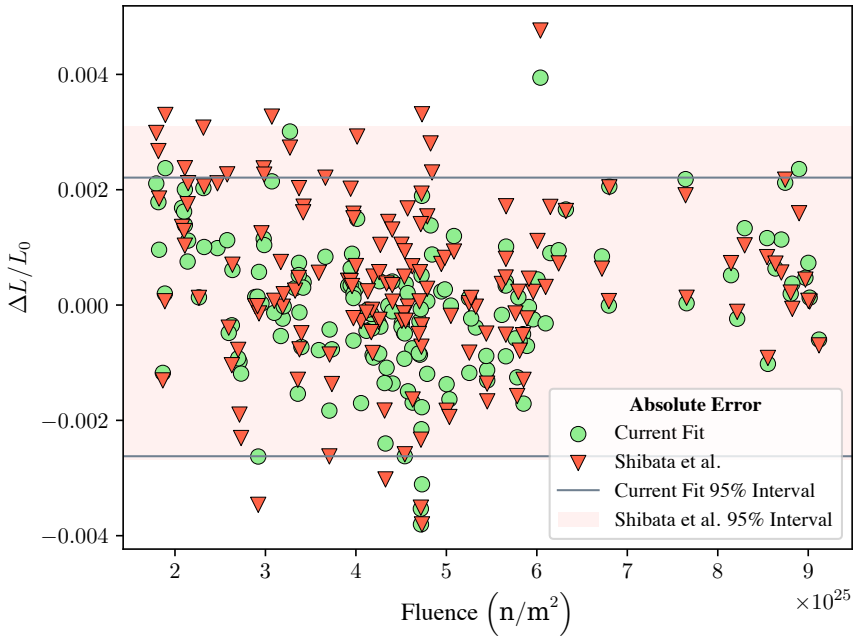

Figure 21: Error comparison between strain prediction from the fit developed in this work and Shibata model with respect to experimental observations of IG-110 graphite.

95% error bounds show that the fit obtained in the current work provides a better prediction of the strain when compared with the experimental data obtained from the AGC campaigns.

For the NBG-18 graphite grade, the same procedure was used to obtain the following expression for irradiation-induced creep:

$$\varepsilon^C = \frac{\sigma}{E_0} - 1.7286 \times 10^{-4} \exp\left(2.73157 \times 10^{-3} T\right) \sigma\gamma \tag{21}$$

where the preirradiation Young's modulus of NBG-18 is given as a Weibull distribution with a mean of 10.44 GPa and a standard deviation of 0.95 GPa [8]. The mean value was used for determining the parameters in this work, and the comparison with experimental data and the errors are shown in Figures 22 and 23, respectively.

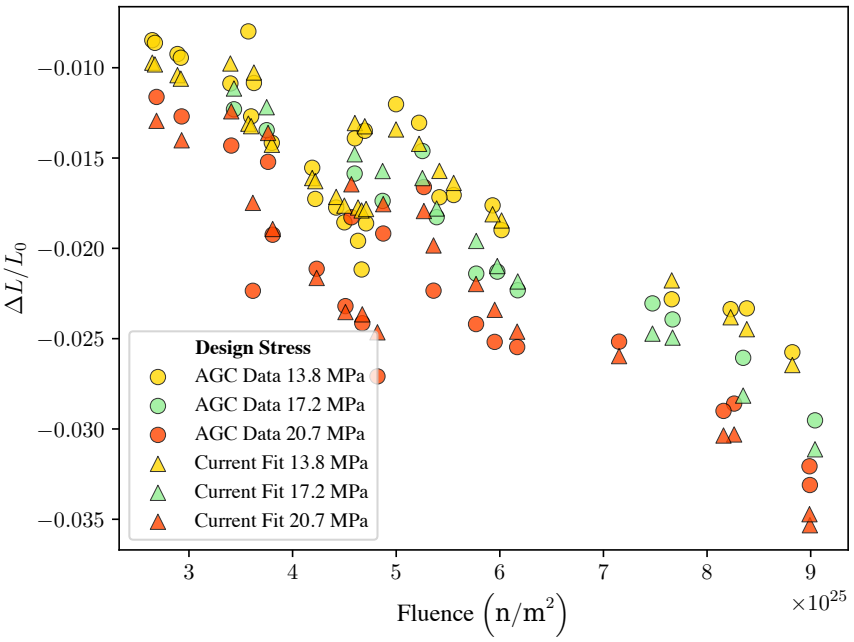

Figure 22: Comparison of the strain predictions with the experimental data for NBG-18 graphite.

2.4.2 Grizzly Simulations

The IG-110 model implemented in Grizzly can be used to simulate the IIDC and irradiation-induced creep, both individually and together, as desired. For IIDC, a `StructuralGraphiteIrradiationEigenstrain` block is added to the input files, with the required parameters for that block, as shown in the example below:

```
[GraphiteGrade_iidc]
      type = StructuralGraphiteIrradiationEigenstrain
      temperature = temperature
      graphite_grade = IG_110
      fluence_conversion_factor =  1.0
      eigenstrain_name = irrad_strain
[]
```

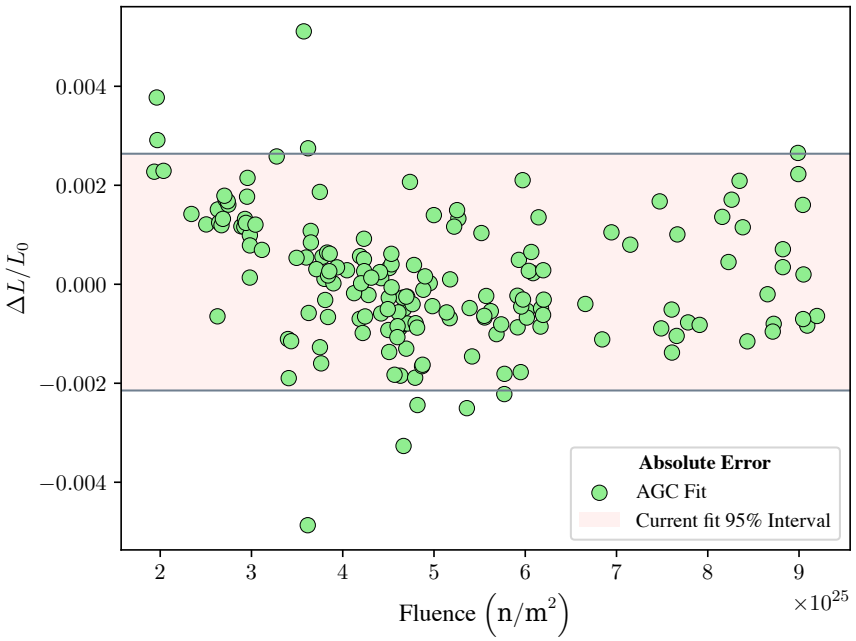

Figure 23: Error comparison of predicted strain with experimental observations of NBG-18 graphite.

For simulating irradiation-induced creep, the user needs to include a `StructuralGraphiteCreepUpdate` block in the input file and specify their choice of models and conditions. A simple example of such a block is shown below:

```
[GraphiteGrade_creep]
      type = StructuralGraphiteCreepUpdate
      graphite_grade = IG_110
      IG_110_model = AGC3
      temperature = 873.15
      creep_scale_factor = 1.0
[]
```

For a compressive strain of 1.0 MPa applied to a simple cube model, the model contracts axially by $1.219\,94 \times 10^{-1}$ %, while it expands transversely by $6.099\,70 \times 10^{-2}$ %. The current implementation assumes that the creep response is represented by J2 theory, which assumes that there is no change in volume during the creep. As a result, the transverse strain is half of the predicted axial strain as expected by conservation laws and the axial results agree closely with predictions from the models developed as part of this work. There is, however, an approximately 7.5 % discrepancy between the simulation and experimental results in the transverse direction. This points to a need for an alternate creep update strategy and this is supported by the net change in volume observed experimentally and as shown in Figures 24 and 25. This is an important area for further investigation.

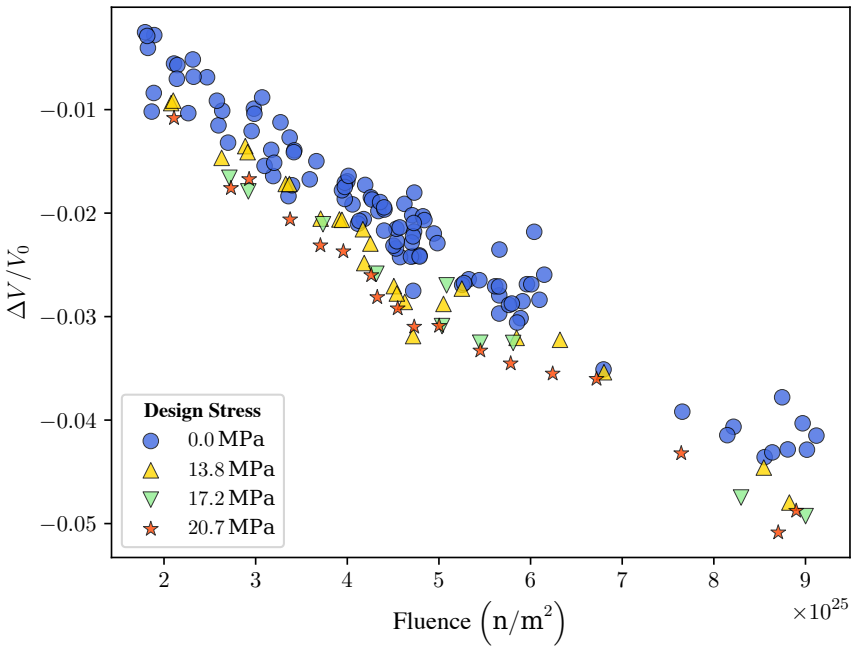

Figure 24: Volumetric strain of the IG-110 graphite samples as measured by AGC 1–3 campaigns.

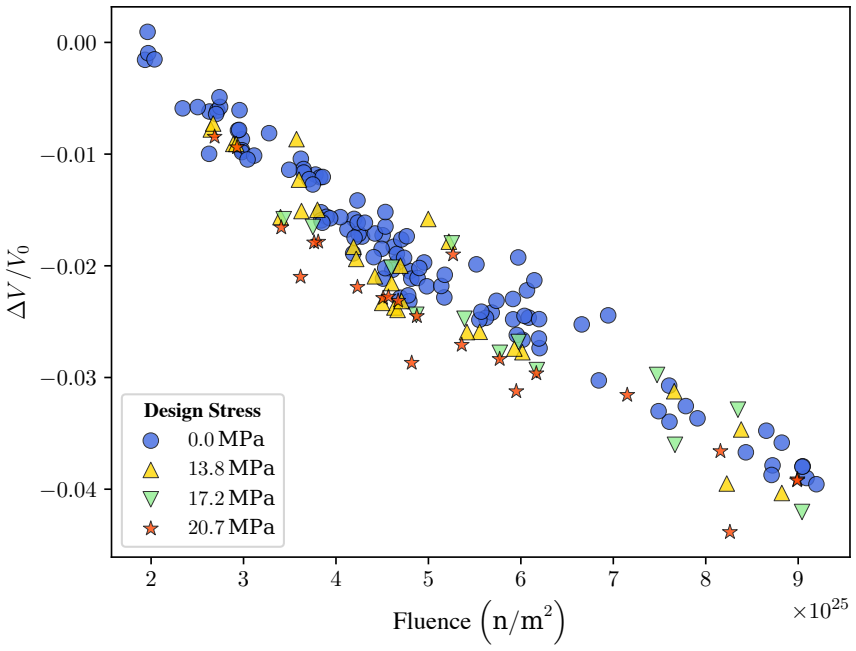

Figure 25: Volumetric strain of the NBG-18 graphite samples as measured by AGC 1–3 campaigns.

3 DAMAGED PLASTICITY MODEL DEVELOPMENT AND APPLICATION

An important part of the suite of tools being developed for graphite modeling is a complete modeling capability for its mechanical response, including nonlinear behavior in both compression and tension. This is necessary for assessing the performance of graphite components in severe loading scenarios. It is also important for interpreting the results of splitting disk tests, which are an attractive method for experimentally characterizing the tensile strength of graphite but present challenges in correlating the measured peak compressive load with the tensile strength.

The mechanical response of graphite has much in common with that of concrete. Both materials are quasibrittle, with significantly more strength and ductility in compression than in tension. Prior work demonstrated the utility of the damaged plasticity model of Lee and Fenves [22] for modeling splitting disk tests. The model had previously been implemented in the BlackBear code, which is an open-source code that provides a subset of Grizzly's capabilities.

While the implementation of the damaged plasticity model showed promise for modeling graphite tests, the previous implementation was found to have a number of discrepancies when compared to behavior published in the literature [22]. To address these issues, the present work thoroughly reviewed and compared the BlackBear implementation of the model with the published formulation. Based on the findings of that study, several critical corrections and improvements were made in the present work. These enhancements include decoupling the calculations of the elastoplastic response and the damage response, implementing undamaged strength functions and their derivatives, modifying the definitions of key constants, and correcting the implementation of the plastic consistency parameter. These modifications have resulted in a more accurate and reliable model.

The effectiveness of these improvements is demonstrated by comparing the results of single-element simulations under uniaxial tension and compression with published results [22]. The single element used for these tests is a 82.6 mm cube. Figure 26 compares the stress-strain responses from the revised BlackBear implementation, the results from the previous BlackBear implementation, and published results under uniaxial tension. Similarly, Figure 27 compares the stress-strain responses under uniaxial compression. In both cases, the results from the new model show improved agreement with the published benchmark results.

Furthermore, the same single-element model as above was subjected to biaxial loading, and the biaxial response is compared with the uniaxial response (as plotted in Figure 26). This comparison as shown in Figure 28 aligns well with the expected behavior shown in [22, 23].

Modeling fracture through continuum strain-softening models, such as the one considered here, is well known to be problematic because the structural-level response can vary with changing mesh density. An important feature of the damaged plasticity model is that it adjusts the softening response to address this issue. To assess this capability, the single-element model used in the previous tests was refined isotropically to produce meshes with eight and 64 elements, and uniaxial tension tests were conducted on these configurations. The resulting stress vs. volume-averaged strain response shown in Figure 29 shows some sensitivity to mesh size, but this is greatly decreased relative to what would be observed without this correction. It is also important to note that the models with refined meshes were more challenging to converge than the single-element case and were eventually terminated due to convergence issues.

One approach to improve robustness of this model, which due to its softening behavior challenges nonlinear solvers, is to employ Duvaut-Lions viscoplastic regularization [24]. This regularization method is defined as follows:

$$\dot{\epsilon}^{vp} = \frac{1}{\mu}\left(\epsilon^{p} - \epsilon^{vp}\right) \tag{22}$$

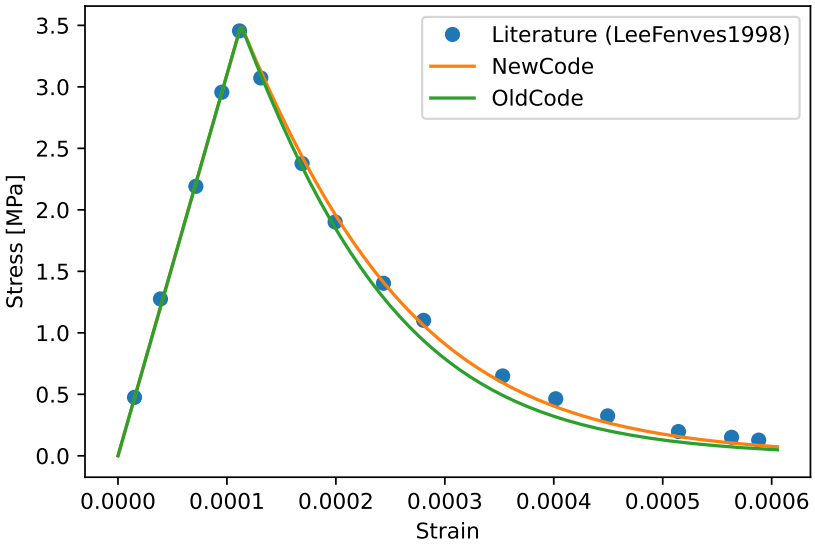

Figure 26: Single-element simulation results under uniaxial tensile loading comparing the updated BlackBear implementation (NewCode) with the prior BlackBear implementation (OldCode) and a published literature solution [22].

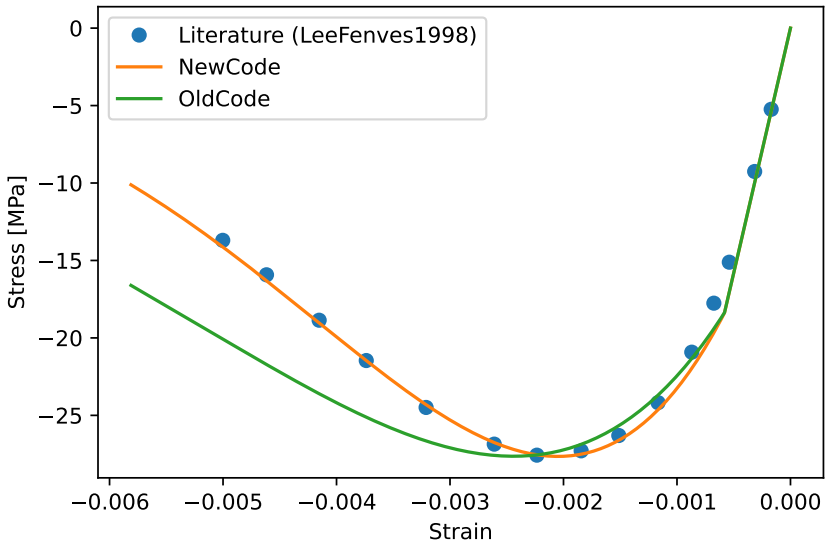

Figure 27: Single-element simulation results under uniaxial compression loading comparing the updated BlackBear implementation (NewCode) with the prior BlackBear implementation (OldCode) and a published literature solution [22].

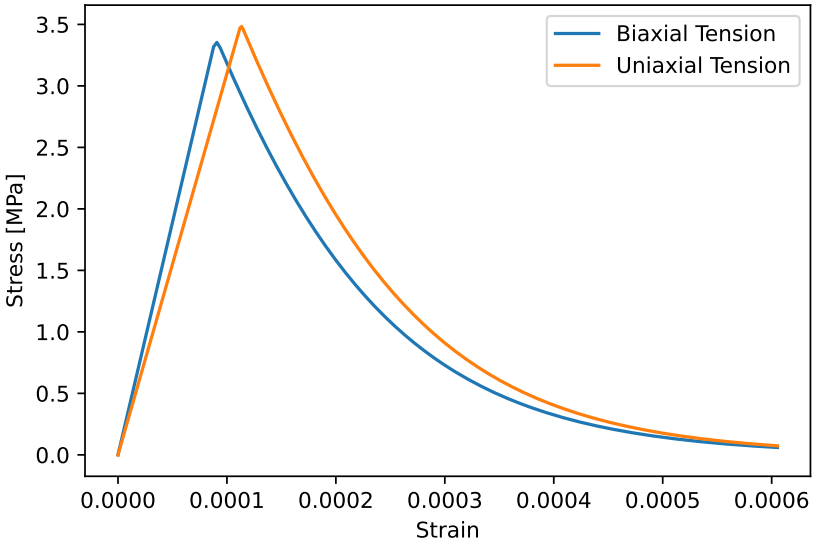

Figure 28: Comparison of a single-element simulation result under biaxial tensile loading with that under uniaxial tensile loading, using the new code.

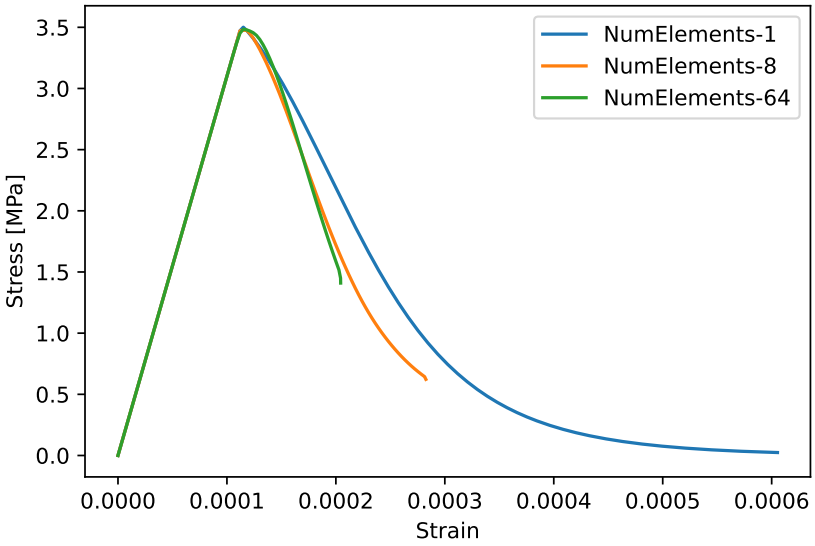

Figure 29: Uniaxial tensile response with varying levels of mesh refinement, using the updated BlackBear implementation.

$$\dot{D}^{vp} = \frac{1}{\mu}(D - D^{vp}) \tag{23}$$

$$\sigma = (1 - D^{vp})\,\overline{\sigma}^{vp} \tag{24}$$

$$\overline{\sigma}^{vp} = C_0 : (\epsilon - \epsilon^{vp}) \tag{25}$$

Here, ϵ^{vp}, D^{vp}, and $\overline{\sigma}^{vp}$ represent the viscoplastic regularized plastic strain, stiffness degradation damage variable, and undamaged stress, respectively. The parameter μ is the viscosity parameter. Additionally, ϵ^{p}, ϵ, C_0, and D represent the plastic strain, total strain, elastic stiffness tensor, and stiffness degradation damage variable, respectively.

A prototype implementation of this regularization approach, which introduces a user-specified amount of artificial viscosity, has been added to the BlackBear implementation of the damaged plasticity model. Initial testing indicates that this improves solution robustness, and this is expected to be incorporated into BlackBear after further testing.

Lastly, to demonstrate the application of the updated damaged plasticity model, a splitting disc test simulation was performed. The experiment and simulation model were described in detail in [3]. The load-displacement curve obtained from the simulation with the updated implementation was compared with that obtained from the previous code. These results, shown in Figure 30, indicate a minor, but noticeable difference in the force vs. displacement curve. Notably, while the simulation using the previous implementation of the model failed to converge before reaching the peak load, the updated implementation was able to capture a small portion of the post-peak response. By using the regularization scheme described above, it is expected that more of the softening response can be captured.

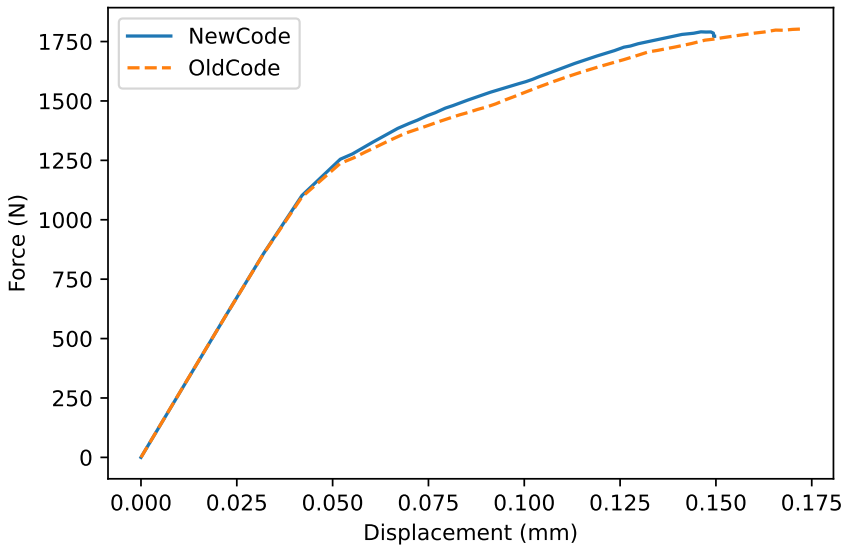

Figure 30: Macroscopic stress-strain response of a splitting disc test.

Figure 31 shows the spatial variation of the damage index in the disc at the end of the simulation. Notably, the damage variable is at its maximum value on the vertical plane near the center of the disc, which suggests a high likelihood of failure by splitting of the disk, starting at its center. The qualitative alignment between the simulation results and the anticipated failure location further demonstrates the model's ability to accurately capture the relevant behavior.

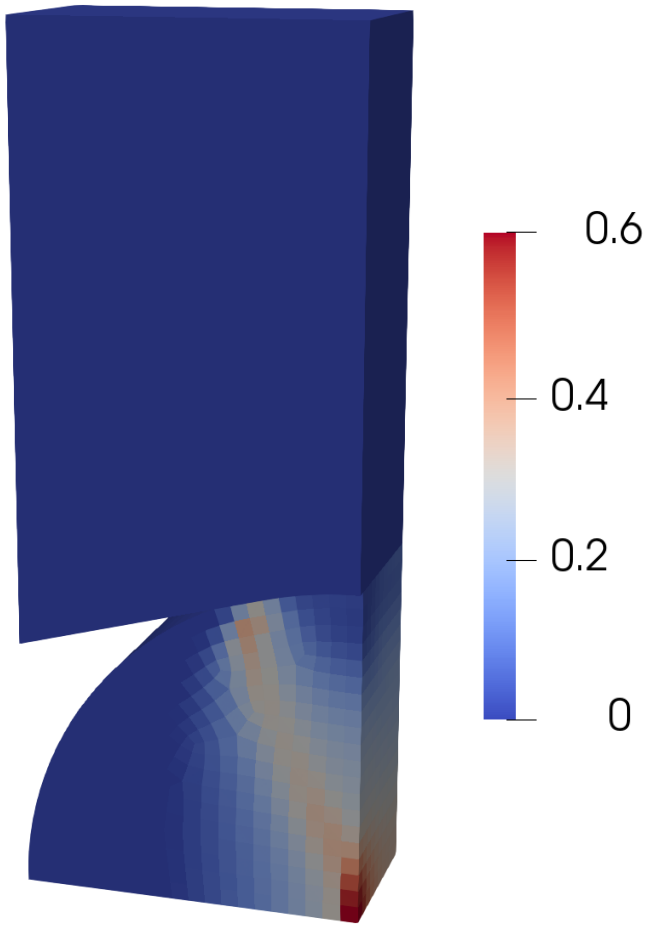

Figure 31: Spatial variation of the damage index computed for the splitting disk model at the peak load.

4 EXTENDED FINITE ELEMENT METHOD DEVELOPMENT

XFEM is a simulation technique that inserts discontinuities at arbitrary locations within a finite-element mesh, which permits mesh-independent modeling of the propagation of discrete cracks. This is attractive for modeling fracture propagation in graphite, and previous work [3] demonstrated the applicability of the XFEM capabilities in MOOSE for graphite simulation. One of the challenges with using XFEM to model fracture in materials such as graphite where multiple cracks could propagate simultaneously is defining the crack locations. To address this issue, in the aforementioned previous work, the algorithms used by the XFEM module in MOOSE to define and grow cracks using fracture integrals were improved. A lower-dimensional cutting mesh, referred to as a `MeshCutter`, was used to mark the locations of the cuts to represent fractures. The `MeshCutter` was then used by the XFEM algorithm to cut the higher-dimensional finite-element mesh. New cracks were permitted to nucleate in elements adjacent to the domain boundary domain by a nucleation algorithm that inserts line segments into the `MeshCutter`.

The current effort builds on the previously developed capabilities to improve the representation of nucleated cracks, allow more generality in the way that cracks can nucleate, and improve the ability to represent propagating cracks in a wider variety of scenarios. Details of these developments are described below.

4.1 Improved Representation of Nucleation on Surfaces

In the original implementation of nucleation with the mesh-based cutter, cracks were permitted to nucleate only in elements adjacent to free surfaces in the finite-element model. Those cracks were nucleated by creating new line segments in the cutting mesh with centers located at the centroids of the finite element. Those line segments needed to be long enough to extend multiple elements into the domain to permit crack extension. As a result, the line segment also extended past the surface outside the model domain. This isn't typically a major issue, but it does cause some confusion and it makes visualizing the crack planes using the cutting mesh somewhat problematic. In some cases, the line segment might also incorrectly extend into material on the other side of the free surface.

To address these issues, the algorithm for crack nucleation on boundaries was updated in the present work so that the cracks nucleated elements on the surface are shifted so that they terminate a small, user-settable, distance beyond the element's free surface. The small distance by which they extend outside the domain is for handling numerical round-off issues to ensure that all element edges intersected by the crack are marked for cutting with XFEM.

4.2 Crack Nucleation in the Bulk

The initial implementation of `MeshCut2DRankTwoTensorNucleation` UserObject only allowed for crack nucleation along boundaries defined by sidesets. This capability was extended in the current work to also include nucleation in the bulk. Cracks are nucleated in the bulk or from the edge of the boundary by a user-specified length, or if no length is specified, a crack is nucleated across a single element.

The new capabilities of the `MeshCut2DRankTwoTensorNucleation` UserObject are demonstrated in the regression test found at:
`moose/modules/xfem/test/tests/nucleation_uo/nucleate_edge_bulk_crack_2d.i`
The simulation setup for this test is shown in Figure 32, which consists a rectangular block of material with a weakened plane across the center where cracks will nucleate. Units for the simulation are somewhat arbitrary

but are based on MPa, cm, and s. The weakened plane has regions of higher and lower nucleation strengths, which will lead to cracks nucleating in the four low-strength regions. The nucleation criterion in this example is based on the maximum principal stress, and a crack will nucleate when the maximum principal stress on the central plane reaches 100, shown by the lowest nucleation value in Figure 32.

The block is incrementally loaded normal to the plane by displacing the nodes highlighted on the top surfaces while holding the bottom surface fixed. The central top nodes are displaced at a slightly higher rate than the top edge nodes, leading to cracks first nucleating in the bulk, as shown in Figure 33b, followed by cracks nucleating on the edges, as shown in Figure 33c. The cracks nucleated in Figure 33c are nucleated along the edge of the domain, and the nucleation length matches those nucleated in the bulk. The nucleated cracks then grow using fracture integrals as the nodes are further displaced, as shown in Figure 33d.

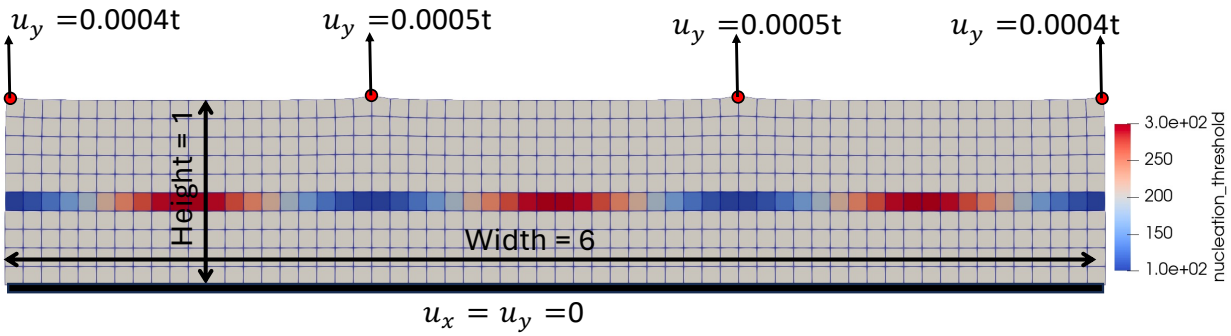

Figure 32: Simulation setup for regression test demonstrating bulk and edge crack nucleation and growth.

4.3 Stress-Based Crack Growth

Fracture integrals are used as a criterion for crack growth and as an indicator for the direction of fracture propagation, because they are based on fracture toughness, which can be characterized experimentally, and because they are relatively independent of mesh size. Fracture integrals are computed based on stresses and strains and evaluated on rings of the domain surrounding the crack tip. This approach works quite well in most cases, except that, as a crack approaches a free surface or another crack, the integration volumes used for computing the fracture integrals can extend beyond the domain, leading to a nonphysical reduction in the computed value of the fracture integral. This can cause crack growth to artificially stop near boundaries, as will be demonstrated in this section.

One approach to address this issue, followed here, is to base crack propagation on either the computed fracture integral or the stress in a region ahead of the crack tip. Because fractures inherently cause singular stress fields ahead of the crack tip, local measures of the stress field are unreliable for use as growth criteria. However, an average of the stress over a finite distance ahead of the crack tip can be used as a reasonable criterion for extending a crack across the remaining ligament between the tip of an advancing crack and a free surface or another crack, because if the average stress over that ligament exceeds the material's tensile strength, that ligament would fail regardless of the nature of the stress concentration at the crack tip.

To use stress as a criterion for growth, in the MOOSE XFEM implementation, a code module was developed to provide computed quantities based on integrating over regions near the crack tip, corresponding to discrete points along a crack front (in three dimensions [3D]) or at the crack tip (in 2D). This module, named `CrackFrontNonlocalStress` is a MOOSE VectorPostprocessor, and the results that it computes are organized in the same way as those computed by the modules that compute fracture integrals in MOOSE.

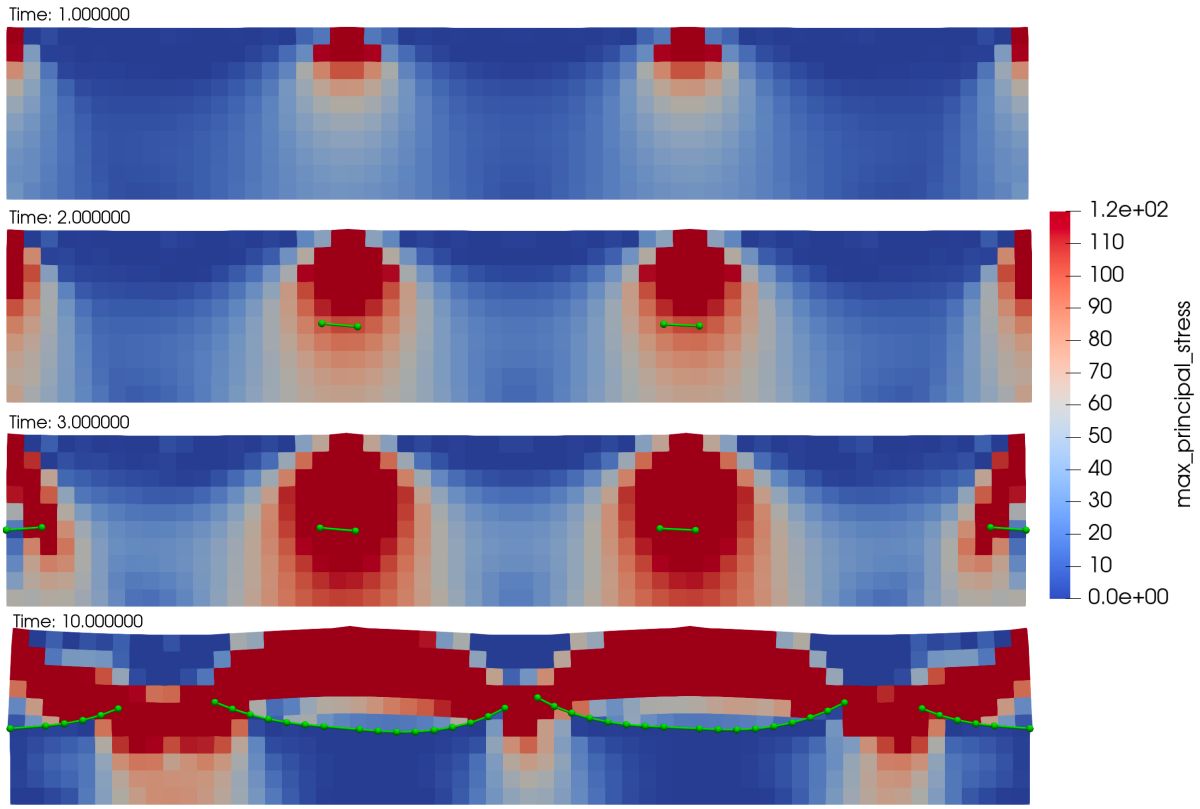

Figure 33: Simulation results for regression test setup shown in Figure 32 at multiple time steps, with times indicated on the top right of each image. Results are colored by maximum principal stress. Time=1: Shows the loading after a single time step, where stress fields below the central load points are slightly higher than those below the edge nodes. Time=2: First cracks are nucleated in the bulk when the maximum principal stress reaches 100. Time=3: Second set of cracks nucleated on the edge. Time=10: Nucleated cracks grow over several time steps using interaction integrals.

Because of this, it is straightforward for the `MeshCut2DFractureUserObject` code module, which defines the crack topology using a lower-dimensional mesh, to obtain both nonlocal averages of the stress ahead of the crack tip and fracture integrals. The `MeshCut2DFractureUserObject` can thus use results from both the `CrackFrontNonlocalStress` VectorPostprocessor and the `InteractionIntegral` VectorPostprocessor to grow cracks. Cracks are propagated when either the computed stress intensity factor exceeds the fracture toughness or the nonlocal average stress exceeds the tensile strength.

Crack growth using `CrackFrontNonlocalStress` is demonstrated in the regression test found in MOOSE at:
`moose/modules/xfem/test/tests/mesh_cut_2D_fracture/edge_crack_2d_propagation.i`
The simulation setup for this test is shown in Figure 34. The mesh is initially cut by the `MeshCutter` using the mesh shown in red. The block of nodes inside the box on the top surface have a prescribed incrementally increasing displacement field, and the bottom surface is held fixed.

Figure 35 shows the final crack length at $t = 3$ for a scenario where the `MeshCut2DFractureUserObject` only uses the `InteractionIntegral` as a criterion for crack growth. Initially, the crack extends on both the left and right tips of the crack, but as the right crack tip approaches the boundary, it stops, even though the stress at the right side of the domain should be high enough to drive this crack tip through the boundary. The

integration domain used for computing the interaction integral is shown by the q-function calculated around the right crack tip in Figure 35b, and it is clear that the inner and outer integration radii, shown by the dashed lines, intersect the free surface.

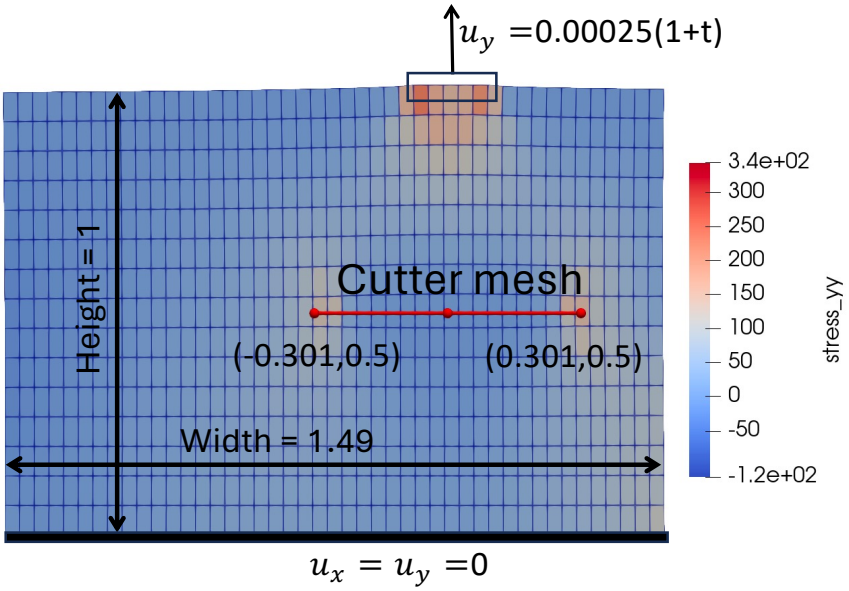

Figure 34: Simulation setup to demonstrate crack growth using interaction integrals and nonlocal stress.

A second variant of this test was set up to compute an average stress ahead of the crack tip using `CrackFrontNonlocalStress`, based on the stress in the direction normal to that of crack extension, denoted as σ_{nn}:

$$\sigma_{nn} = \boldsymbol{n} \cdot \boldsymbol{\sigma} \cdot \boldsymbol{n} \tag{26}$$

where $\boldsymbol{n}$ is the normal vector to the direction of crack extension. This stress is averaged over the box volume shown in Figure 35a to provide a nonlocal value that should be less prone to local element level fluctuations in the stress field at the XFEM crack tip. $\bar{\sigma}_{nn}$ is the stress value averaged over the semitransparent boxes shown at each crack tip in Figure 35a. The averaging box is centered on the crack front, oriented in the crack front direction, and should be large enough to cover a few elements in each direction but not too large as to dilute the values. A tall skinny box like the one used here captures the high crack tip normal stress for a crack under mode-I loading.

The quantity computed by the `CrackFrontNonlocalStress` VectorPostprocessor is then used by the `MeshCut2DFractureUserObject` in the following criterion for crack growth:

$$\sigma_c \leq \bar{\sigma}_{nn} \tag{27}$$

where σ_c is a critical stress normal to the crack face. Currently, if the crack propagates due to exceeding this criterion, it will only extend along the direction of the line segment at the crack tip. This could be generalized in the future to allow the crack to curve under mixed-mode loading.

Figure 36a shows the final crack configuration when a combination of the `InteractionIntegral` and `CrackFrontNonlocalStress` growth criteria is used by the `MeshCut2DFractureUserObject`. This simulation uses $\sigma_c = 120$, and based on the stress values plotted in Figure 35a, the stresses are high enough that the crack should grow into the ligament. The `CrackFrontNonlocalStress` growth criterion causes both crack tips to grow past the end points computed in the simulation previously shown in Figure 35, which only used

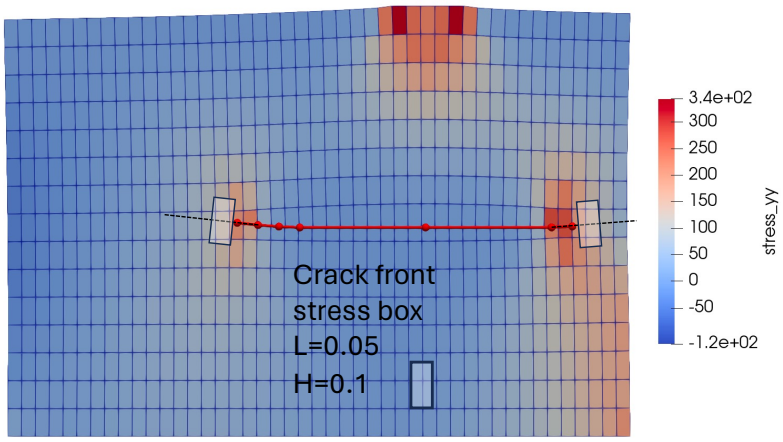

a) t=3, Stress normal to crack

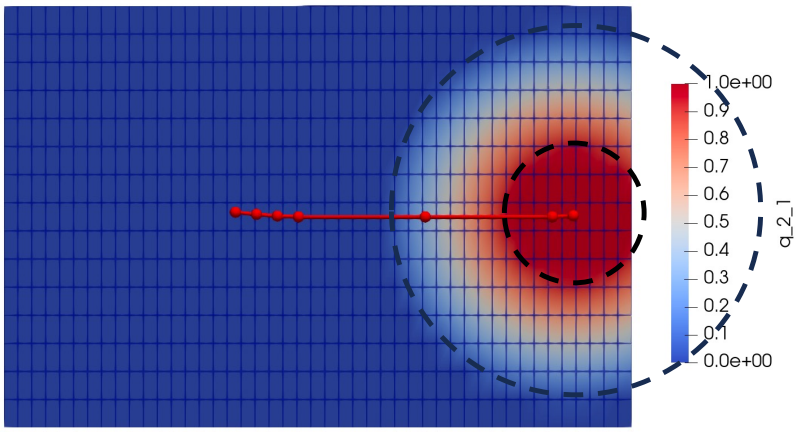

b) t=3, Fracture integral q-function

Figure 35: Final crack configuration for crack growth in a test case using only the interaction integral as a criterion for crack propagation. a) The stress field normal to the crack tip. The semitransparent boxes at each crack tip are the averaging volumes used for computing the average crack tip stress. The stress box at the bottom is shown for reference to indicate its size relative to that of the finite elements used in the simulation. b) The q-function used for computing the interaction integral for the crack tip on the right side of the model, with inner and outer radii shown by the dashed lines.

the interaction integral for crack growth. Because the system is designed to propagate the crack if either of the criteria are met, the value for σ_c should be set large enough that crack growth is only governed by the nonlocal stress criterion near boundaries and not in the bulk.

Figure 36b shows a comparison of the final crack configurations of the combined interaction integral and nonlocal stress criterion in green versus the interaction integral shown by the red points. This figure shows the cracks initially following a similar growth path using the interaction integral criterion. Once the interaction integral decreases near the boundary, the nonlocal stress criterion causes the green crack to continue to grow. The green crack growth using the nonlocal stress criterion is in a straight line.

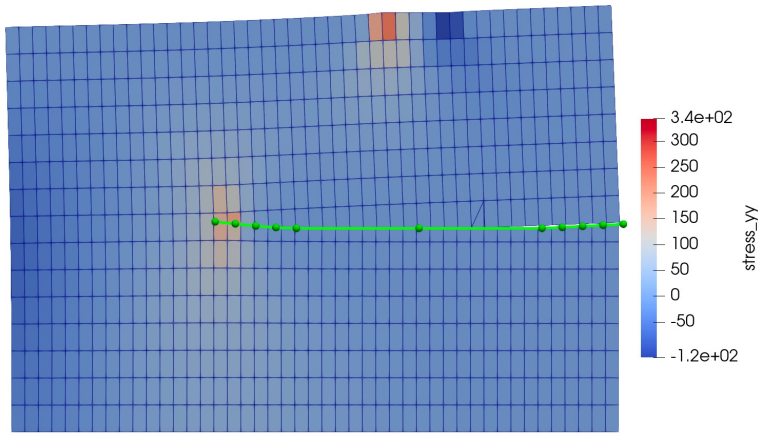

a) t=3, Fracture integral & stress growth

b) Comparing final MeshCutter crack configurations.

Figure 36: a) Final crack configuration for crack growth using the combination of the interaction integral and nonlocal stress. b) Comparison of final crack configurations for growth using only the interaction integral in red and the combined interaction integral and nonlocal stress in green.

5 SUMMARY AND FUTURE WORK

This report summarizes the further development of simulation capabilities for predicting the performance of nuclear-grade graphite, which build on previous efforts. Capabilities have been developed in MOOSE, Grizzly, and BlackBear to model thermal response and nonlinear mechanical behavior in graphite components. A major part of this effort was developing graphite creep models for high-temperature and radiation environments. A full set of thermal and mechanical models for capturing the long-term inelastic creep deformation under irradiation conditions for the IG-110, NBG-19, and H-451 graphite grades in Grizzly. This included implementing models for the thermal and elastic properties of NBG-18 based on expressions available in literature. Models were also implemented for irradiation-induced dimensional change and irradiation-induced creep for the IG-110 and NBG-18 grades. To do this, expressions were fit to experimental data from the AGC program. This effort has resulted in a repeatable method for developing irradiation-induced swelling and creep models based on experimental data that can be applied to new graphite grades as experimental data become available. The models developed here are limited to the range of fluence in the tests from the experimental program. As more data becomes available, these models can be updated to predict the response under longer-term exposure to reactor conditions. In addition, experimental data is available for additional graphite grades of current interest, and models can be developed for those grades. One important area for future investigation is the appropriate approach for capturing volumetric strain. The current implementation of the creep models employs J2 theory, which assumes that creep strains are entirely distortional. Testing on the grades considered here indicated that there is some discrepancy between the experimental and simulated behavior because the experiments show some volumetric strain. Additionally, there is significant spread in the experimental data, and further work is needed to characterize the uncertainty in the functional forms used to represent the material response.

Another major part of this effort was the continued development of nonlinear models for quasibrittle material in BlackBear that were initially developed for concrete but, after reparameterization, are also applicable to graphite. Some discrepancies exist between the initial implementation of that model in BlackBear and published benchmark results. To address these, the BlackBear implementation of the model was thoroughly reviewed and revised to make it more consistent with the published model. The improved consistency of the revised model with published benchmark solutions was demonstrated, and the revised model was successfully applied to simulate a splitting-disk test. In addition, an initial implementation of a viscoplastic regularization technique, which is expected to improve solution robustness of the model, was developed. Further testing on larger-scale problems is needed to assess the robustness of the damaged plasticity model with regularization. Extensive experimental data on splitting tension tests is available and can be used for validating this model for multiple graphite grades.

Finally, the capabilities of the XFEM implementation in MOOSE have been improved. The mesh-based cutting approach can now be used to represent cracks that nucleate in either the bulk or on the surface of a domain. In addition, the capability to nucleate cracks in elements on the surface has been improved, and previously identified issues with extending cracks near the edge of a domain or another crack have been addressed by implementing a nonlocal stress computation that can be used in conjunction with fracture integrals. These capabilities have been demonstrated on simple problems. These still need to be tested on component-scale problems that potentially contain multiple cracks and validated against experimental data. Future work should also focus on the 3D XFEM capability. Previous 3D simulation work [3] used the smeared cracking model to capture failure in thick graphite components, but XFEM has important advantages over such approaches. The current XFEM capability works in 3D, but the algorithms for capturing crack nucleation, growth, and intersection in 3D still need additional work. Physics occurring on the XFEM cut interfaces should also be captured to predict different modes of failure through cohesive laws or different

physical mechanisms, such as surface corrosion.

Another important area not addressed here that still needs work is addressing the effect of specimen size on apparent fracture strength. The fracture modeling techniques developed in this program provide some of the tools to address this need, but further work is necessary to develop predictive models that correctly account for these size effects and validate those models against experimental data.

REFERENCES

[1] B. W. Spencer, W. M. Hoffman, S. Biswas, W. Jiang, A. Giorla, and M. A. Backman, "Grizzly and BlackBear: Structural component aging simulation codes," *Nuclear Technology*, vol. 207, pp. 981–1003, Apr. 2021.

[2] G. Giudicelli, A. Lindsay, L. Harbour, C. Icenhour, M. Li, J. E. Hansel, P. German, P. Behne, O. Marin, R. H. Stogner, J. M. Miller, D. Schwen, Y. Wang, L. Munday, S. Schunert, B. W. Spencer, D. Yushu, A. Recuero, Z. M. Prince, M. Nezdyur, T. Hu, Y. Miao, Y. S. Jung, C. Matthews, A. Novak, B. Langley, T. Truster, N. Nobre, B. Alger, D. Andrs, F. Kong, R. Carlsen, A. E. Slaughter, J. W. Peterson, D. Gaston, and C. Permann, "3.0 - MOOSE: Enabling massively parallel multiphysics simulations," *SoftwareX*, vol. 26, p. 101690, May 2024.

[3] B. W. Spencer, L. B. Munday, G. Singh, and V. Prithivirajan, "Initial fracture propagation modeling of graphite components with Grizzly," Tech. Rep. INL/RPT-23-74062, Idaho National Laboratory, Idaho Falls, ID, June 2023.

[4] W. Windes, W. D. Swank, D. Rohrbaugh, and J. Lord, "AGC-2 graphite preirradiation data analysis report," Tech. Rep. INL/EXT-13-28612, Idaho National Laboratory, Idaho Falls, ID, United States, 2013.

[5] G. Vasudevamurthy, T. Byun, P. Pappano, L. Snead, and T. Burchell, "Effect of specimen size and grain orientation on the mechanical and physical properties of NBG-18 nuclear graphite," *Journal of Nuclear Materials*, vol. 462, pp. 1–7, 2015.

[6] X. Zhou, H. Wang, and S. Yu, "Anisotropy of coefficient of thermal expansion of nuclear graphite under compressive stresses," *Nuclear Engineering and Design*, vol. 241, no. 3, pp. 752–754, 2011. The International Conference on Structural Mechanics in Reactor Technology (SMiRT19) Special Section.

[7] M. Srinivasan, B. Marsden, W. von Lensa, L. Cronise, and R. Turk, "Appendices to the assessment of graphite properties and degradation, including source dependence," Tech. Rep. TLR/RES/DE/REB-2021-08, U.S. Nuclear Regulatory Commission, August 2021.

[8] M. C. Carroll, W. E. Windes, D. T. Rohrbaugh, J. P. Strizak, and T. D. Burchell, "Leveraging comprehensive baseline datasets to quantify property variability in nuclear-grade graphites," *Nuclear Engineering and Design*, vol. 307, pp. 77–85, 2016.

[9] W. E. Windes, D. T. Rohrbaugh, W. D. Swank, and D. L. Cottle, "AGC-3 specimen post-irradiation examination data package report," Tech. Rep. INL/EXT-17-43823, Idaho National Laboratory, 12 2017.

[10] American Society of Mecahnical Engineers, "Section III. Rules for Construction of Nuclear Facility Components. Division 5. High Temperature Reactors," Tech. Rep. ASME BPVC.III.5-2023, ASME Boiler and Pressure Vessel Code, 2023.

[11] A. A. Campbell and T. D. Burchell, "Radiation effects in graphite," in *Comprehensive Nuclear Materials* (R. J. Konings and R. E. Stoller, eds.), pp. 398–436, Oxford: Elsevier, second edition ed., 2020.

[12] F. Banhart, "Irradiation effects in carbon nanostructures," *Reports on Progress in Physics*, vol. 62, no. 8, p. 1181, 1999.

[13] K. Urita, K. Suenaga, T. Sugai, H. Shinohara, and S. Iijima, "In situ observation of thermal relaxation of interstitial-vacancy pair defects in a graphite gap," *Phys. Rev. Lett.*, vol. 94, p. 155502, Apr 2005.

[14] R. H. Telling and M. I. Heggie, "Radiation defects in graphite," *Philosophical Magazine*, vol. 87, no. 31, pp. 4797–4846, 2007.

[15] J. H. W. Simmons, *Radiation damage in graphite: international series of monographs in nuclear energy*, vol. 102. Elsevier, 2013.

[16] J. Brocklehurst and B. Kelly, "Analysis of the dimensional changes and structural changes in polycrystalline graphite under fast neutron irradiation," *Carbon*, vol. 31, no. 1, pp. 155–178, 1993.

[17] B. Kelly and T. Burchell, "Structure-related property changes in polycrystalline graphite under neutron irradiation," *Carbon*, vol. 32, no. 3, pp. 499–505, 1994.

[18] T. Shibata, M. Eto, E. Kunimoto, S. Shiozawa, K. Sawa, T. Oku, and T. Maruyama, "Draft of standard for graphite core components in high temperature gas-cooled reactor," Technical Report JAEA-Research 2009-042, Japan Atomic Energy Agency, 01 2010.

[19] B. T. Kelly and A. J. E. Foreman, "The theory of irradiation creep in reactor graphite – The dislocation pinning-unpinning model," *Carbon*, vol. 12, no. 2, pp. 151–158, 1974.

[20] D. Martin and R. Henson, "The scattering of long wavelength neutrons by defects in neutron-irradiated graphite," *Philosophical Magazine*, vol. 9, no. 100, pp. 659–672, 1964.

[21] L. L. Snead, C. I. Contescu, T. S. Byun, and W. Porter, "Thermophysical property and pore structure evolution in stressed and non-stressed neutron irradiated IG-110 nuclear graphite," *Journal of Nuclear Materials*, vol. 476, pp. 102–109, 2016.

[22] J. Lee and G. L. Fenves, "Plastic-Damage Model for Cyclic Loading of Concrete Structures," *Journal of Engineering Mechanics*, vol. 124, pp. 892–900, Aug. 1998.

[23] J. Lee, *Theory and implementation of plastic-damage model for concrete structures under cyclic and dynamic loading*. Dissertation, University of California, Berkeley, 1996.

[24] O. Omidi and V. Lotfi, "Continuum large cracking in a rate-dependent plastic-damage model for cyclic-loaded concrete structures," *International Journal for Numerical and Analytical Methods in Geomechanics*, vol. 37, no. 10, pp. 1363–1390, 2013.